Science Advances
AAAS

Supplementary Materials for

Imaging of the electronic bonding of diamond at pressures up to 2 million atmospheres

Sung Keun Lee *et al.*

Corresponding author: Sung Keun Lee, sungklee@snu.ac.kr

Sci. Adv. **9**, eadg4159 (2023)
DOI: 10.1126/sciadv.adg4159

This PDF file includes:

Supplementary texts A to G
Figs. S1 to S29
Tables S1 to S6
References

A. Additional Experimental and Computational details

IXS collection. The modified panoramic DAC with a large side opening was mounted on a multi-axis goniometer. Energy resolution is approximately 1.4 eV. The monochrometer is a Si(111) double-crystal with FWHM with 5(h)×3(v) μm^2 that were achieved by a pin-hole and a KB mirror pair. The analyzer is spherical Si(555) crystal [see (*28, 29, 50*) for the details]. The carbon K-edge spectra were collected with a fixed scattering angle of 25° and Bragg angle for the analyzer of 90°. The scattered X-rays were collimated by the poly-capillary post-sample collimator with a 7 mm working distance (i.e., from sample to input end of poly-capillary) and were transmitted to the Si(555) analyzer. The input field of view for the poly-capillary post-sample collimator is ~35 μm diameter, resulting in a spatial resolution of ~75 μm along the X-ray paths. The sampled volume for the current IXS setup is ~75×5×3 (D×H×V) μm^3. In order to collect the two-dimensional IXS image of the compressed diamond, the position of the DAC was systematically varied. The IXS spectrum was collected at each point. The background was constrained from the pre-edge intensity and subtracted to yield the spectra presented in the current manuscript. See (*28, 29*) and references therein for further details. As shown in Figure S1, for the current IXS experiment setup, the diamond is under uniaxial compression. The scattering geometry of the current experiment selectively probes the electronic structure (DOS) perpendicular to the compression direction ([001], $q \perp c$).

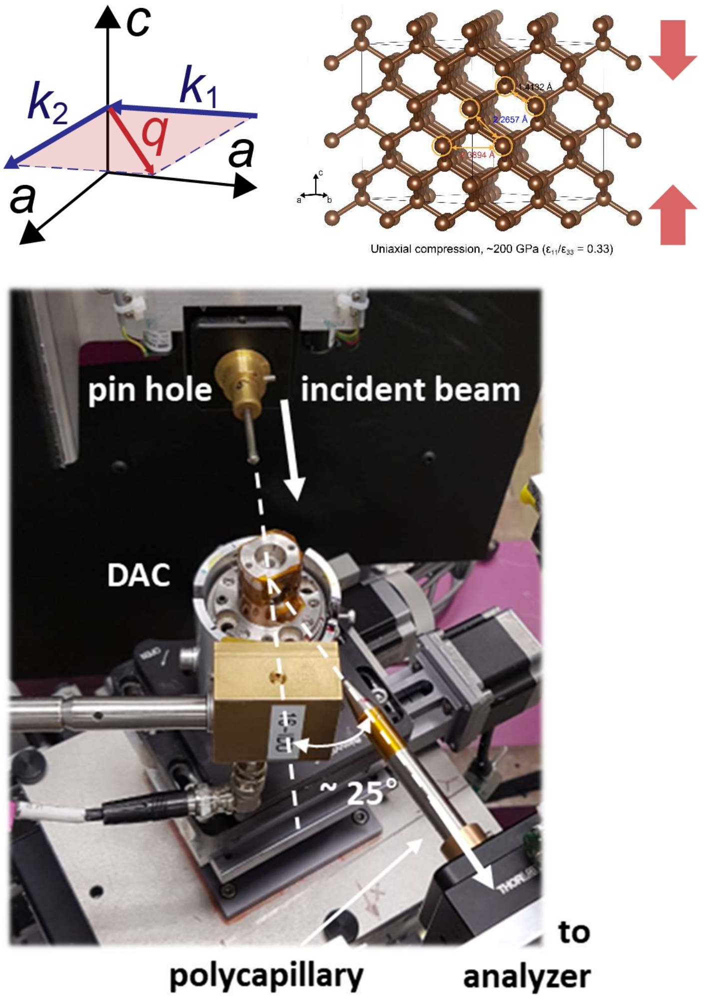

Fig. S1. **The IXS setup and scattering geometry ($q \perp c$) to image the electronic structures of the deformed diamond anvil.** The scattering angle was fixed to 25°.

***Ab initio* calculations.** We used the on-the-fly generated (OTFG) pseudopotential to describe the electronic interactions with a cutoff energy of 800 eV, as the convergence was achieved with a cutoff energy > ~600 eV. The PBE exchange-correlation functional was used to calculate the electron-electron correlations (*53*). The Monkhorst-Pack *k* point grid of 6×6×6 with the number of irreducible *k* points of 108 was used. The energy convergence of self-consistent field calculations is 5.0×10^{-7} eV/atom (See (*24, 30, 54*) and references therein). While the semi-empirical dispersion correction may be necessary to predict the lattice parameters of graphite accurately (*55*), the IXS features for diamond, calculated with and without the dispersion correction, do not show any noticeable spectral difference.

The carbon *K*-edge IXS spectra of compressed diamonds were calculated by applying the final state approximation, where the atomic orbital configuration of the target carbon atom is modified from $1s^2\ 2s^2\ 2p^2$ to $1s^1\ 2s^2\ 2p^2$ to describe the empty core states [See (*24, 54, 56*) and references therein]. The calculations of IXS spectrum with varying supercell size show that the 2×2×2 supercell structure provides converged IXS features, successfully reproducing experimental spectra.

As for the pseudopotential-based DFT calculations, the contribution from core-level excitation should be taken into consideration to estimate the K-edge onset energy because the electronic interactions are represented with the pseudized valence electrons (*52, 57*). In the current study, the transition energy of core electron (E_T) was estimated from the total energy difference between excited and ground states for valence ($\Delta E_\mathrm{valence}$), also considering core orbital contribution (ΔE_core):

$$E_\mathrm{T} = \Delta E_\mathrm{valence} + \Delta E_\mathrm{core} \tag{S1}$$

Here, ΔE_core was estimated from the following relationship:

$$\Delta E_\mathrm{core} = \Delta E_\mathrm{AE\text{-}atom} - \Delta E_\mathrm{PP\text{-}atom} \tag{S2}$$

where $\Delta E_\mathrm{PP\text{-}atom}$ and $\Delta E_\mathrm{AE\text{-}atom}$ and are the energy difference between excited and ground states of a single isolated carbon atom estimated from the pseudopotential and the all-electron calculations [See (*58*) for further details]. The calculated $\Delta E_\mathrm{AE\text{-}atom}$ and $\Delta E_\mathrm{PP\text{-}atom}$ are 304.38 eV and -93.34 eV, respectively. The $\Delta E_\mathrm{valence}$ of compressed diamonds varies from -107.60 eV to -107.87 eV. Consequently, the E_T of carbon atoms in diamond slightly decrease from 290.12 eV to 289.85 eV upon compression. Calculated carbon *K*-edge IXS spectrum was shifted by the corresponding E_T value. The estimated core-level shift of ~0.2-0.3 eV is comparable to the experimental uncertainty. Finally, the calculated spectrum at 1 atm was further shifted (~ 6 eV) to find a good match with experimental IXS spectrum.

B. Effect of pressure on calculated IXS spectra for diamond under hydrostatic compression

The diamond structure (space group Fd$\bar{3}$m) exhibits two overlapping face-centered-cubic (FCC) lattices (*59*). As the equation of state (EOS) for the diamond based on diffraction and *ab initio* calculations are not available beyond 140 GPa (*37*), we extended the EOS to 200 GPa by reducing its molar volume isotropically. Hydrostatic pressure for diamond was also calculated from the diagonal components of the stress tensor. The pressure values from the extended EOS (blue) are somewhat smaller than those calculated from the internal stress (red) (Figure S2). In the current study, we used both pressure values (i.e., calculated and extended EOS) to show the effect of pressure on the peak shift of the σ* feature.

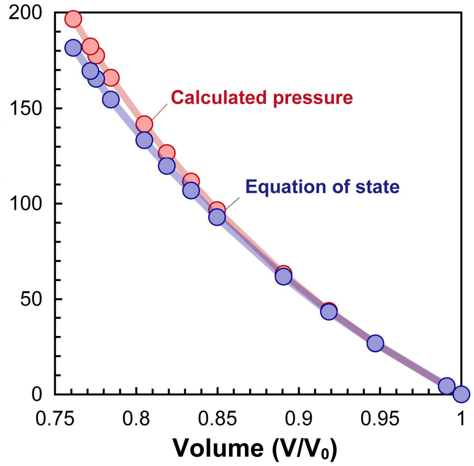

Fig. S2. **Pressure-volume relationships of the compressed diamonds determined from the internal stresses (blue) and from the extended equation of states (red) (*37*).**

Figure S3-left shows the calculated carbon K-edge IXS spectra for diamond under hydrostatic compression up to 2 Mbar. As pressure increases, C-C bond length [d(C-C)] decreases. This results in a higher-energy shift of the peak positions of the edge features (From P1 to P4) (Figure S3-right). The pressure-driven peak shift can be described by the following equation: edge peak position (P) = -A*P + B, with A and B values for the features shown in Table S1. We note that the intensity between the experimental and theoretical calculations are somewhat different, as the latter underestimates the overall intensity at higher energy features. The reason for the difference has been described in our earlier studies of IXS calculations [see (*24, 30, 54*) and references therein]. An observed σ^* peak shift in hydrostatically compressed diamond up to ~2 Mbar corresponds to a decrease in d(C-C) of ~0.1343 Å (Figure 2). It should also be noted that the current IXS experimental setup results in an anisotropic compression of the diamond anvil. Therefore, we also performed *ab initio* calculations of the electronic bandgap and IXS patterns of the uniaxially compressed diamond in the following section (Supplementary Materials C below for detailed calculations protocols and results).

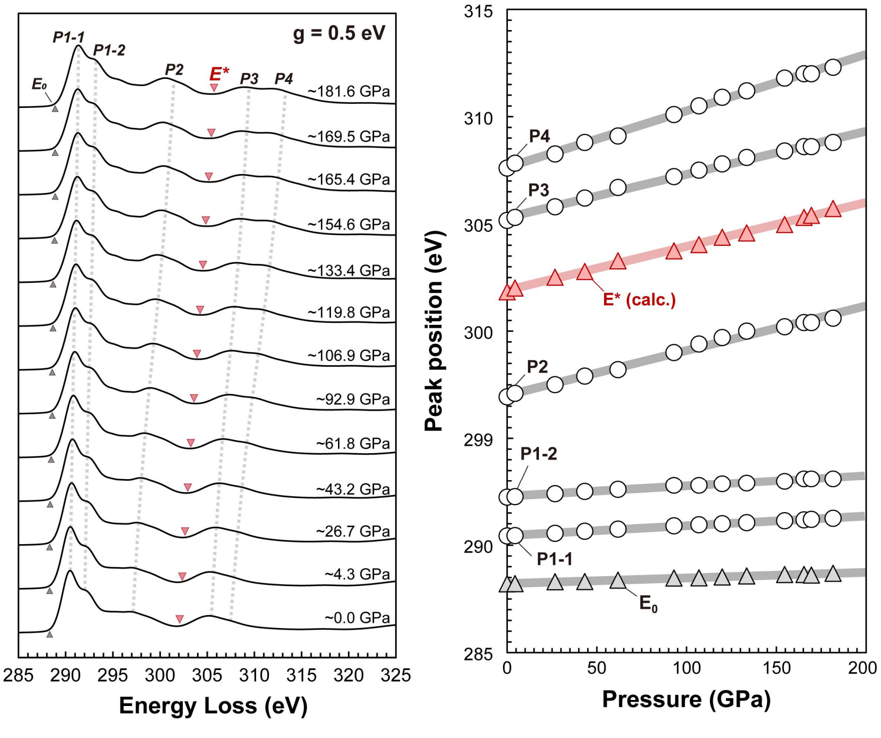

Fig. S3. **Calculated carbon K-edge IXS spectral patterns for diamond with varying pressures. Left. Calculated carbon K-edge IXS spectra for diamond with varying pressures** as labeled. Characteristic peaks (P1–P4) are labeled. The Gaussian broadening factors are 0.5 eV (right) and 0.2 eV (left). **Right.** Effect of pressure on edge onset energy (E_0), 2nd band gap (E*), and characteristic peak positions of the σ^* pattern.

Table S1. The linear relationships between σ* peak positions (eV) from the experimental IXS spectra *vs.* pressure (GPa)

	Peak position (Y) vs. Pressure (X)
P1	$Y = 0.0056 \times X + 291.2$ ($R^2 = 0.999$)
Center of gravity (E_c)	$Y = 0.0176 \times X + 297.0$ ($R^2 = 0.999$)
P2	$Y = 0.0180 \times X + 297.6$ ($R^2 = 0.997$)
E*	$Y = 0.0168 \times X + 301.9$ ($R^2 = 0.999$)
P3	$Y = 0.0171 \times X + 304.9$ ($R^2 = 0.999$)
P4	$Y = 0.0252 \times X + 307.5$ ($R^2 = 0.998$)

Table S2. The linear relationships between calculated σ* peak positions (eV) of the hydrostatically compressed diamond *vs.* pressure (GPa) and peak positions *vs.* C-C bond length (d_{C-C}) (Å)

	Peak position (Y) vs. Pressure (X)	**Peak position (Y) vs. d_{C-C} (X)**
P1-1	$Y = 0.0045 \times X + 290.5$ ($R^2 = 0.996$)	$Y = -6.126 \times X + 299.9$ ($R^2 = 0.997$)
P1-2	$Y = 0.0048 \times X + 292.3$ ($R^2 = 0.987$)	$Y = -6.597 \times X + 302.4$ ($R^2 = 0.993$)
P2	$Y = 0.0208 \times X + 297.0$ ($R^2 = 0.991$)	$Y = -28.233 \times X + 340.4$ ($R^2 = 0.992$)
E*	$Y = 0.0205 \times X + 301.9$ ($R^2 = 0.998$)	$Y = -27.647 \times X + 344.4$ ($R^2 = 0.986$)
P3	$Y = 0.0201 \times X + 305.3$ ($R^2 = 0.994$)	$Y = -27.356 \times X + 347.3$ ($R^2 = 0.997$)
P4	$Y = 0.0263 \times X + 307.6$ ($R^2 = 0.997$)	$Y = -35.594 \times X + 362.4$ ($R^2 = 0.988$)

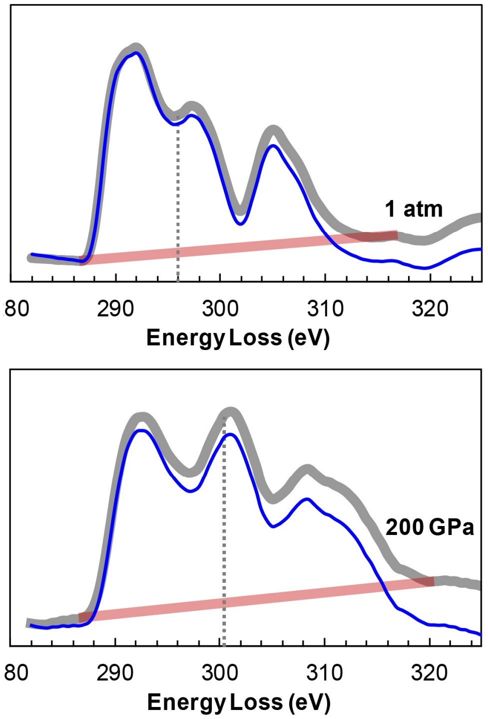

Center of gravity. The center of gravity (E_c) of the C K-edge IXS spectra for the compressed diamond in the current study allows us to compare the pressure-driven spectral evolution of diamonds with those for crystalline and amorphous oxides from earlier IXS studies (e.g., (*24, 28, 29*)). Figure S4 presents procedures as to how E_c was determined from the XRS spectrum. First, we subtract a linear background. Second, we calculated the spectral intensity of the spectra, from which the E_c of the total spectrum can be estimated (see (*24*) for detailed procedures).

Fig. S4. **Estimation of center of gravity (dotted line) of the C K-edge XRS spectra for diamond at 1 atm and 200 GPa**. The grey and blue spectra show the experimental IXS spectra prior to and after background subtraction.

C. Calculations of the electronic structures (bandgap and IXS spectral patterns) of anisotropically compressed diamond at high pressure

C1. Construction of lattice structures of uniaxially compressed diamond

C2. Effect of uniaxial compression on the bandgap of diamond at high pressure (hydrostatic *vs.* uniaxial compression)

C3. Effect of anisotropic compression on the C-C bond distance in compressed diamond (hydrostatic *vs.* uniaxial compression)

C4. Effect of uniaxial compression on the IXS patterns of compressed diamond at high pressure (hydrostatic *vs.* uniaxial compression)

C5. Effect of scattering geometry on the IXS patterns of compressed diamond at high pressure (scattering vector parallel to compression axis *vs.* scattering vector perpendicular to compression axis)

C6. Comparison of compressed diamond at high pressure with experimental IXS spectra

C1. Construction of lattice structures of uniaxially compressed diamond.

We explored the electronic structures of both hydrostatically compressed diamond (labled 'H') (supplemnatry materials above) and investigated two distinct cases of anisotropic compression. As the contraction in the a-a plane in diamond during uniaxial compression is expected to be smaller than that in the c-plane, our calculations take such anisotropy into consideration; in particular, S2 refers to uniaxial compression with anisotropy, as described in an earlier theoretical (*60*) and experimental studies (*20, 61*). Stain-1 (S1) represents an intermediate strain between H and S2. Figure S5-left shows the pressure-induced change in diamond lattice parameters with varying degrees of uniaxial compression. As S2 is characterized as having the largest degree of uniaxial compression (S2>S1>H), more prevalent shortening in the c-axis is shown [i.e., c(S2)< c(S1)]. Note also that lattice parameter a under hydrostatic compression [a(H)] is smaller than that of a(S1) and a(S2) but larger than that of c(S1) and c(S2). This difference results in characteristic pressure-induced changes in c and a for H, S1, and S2 (Figure S5-right).

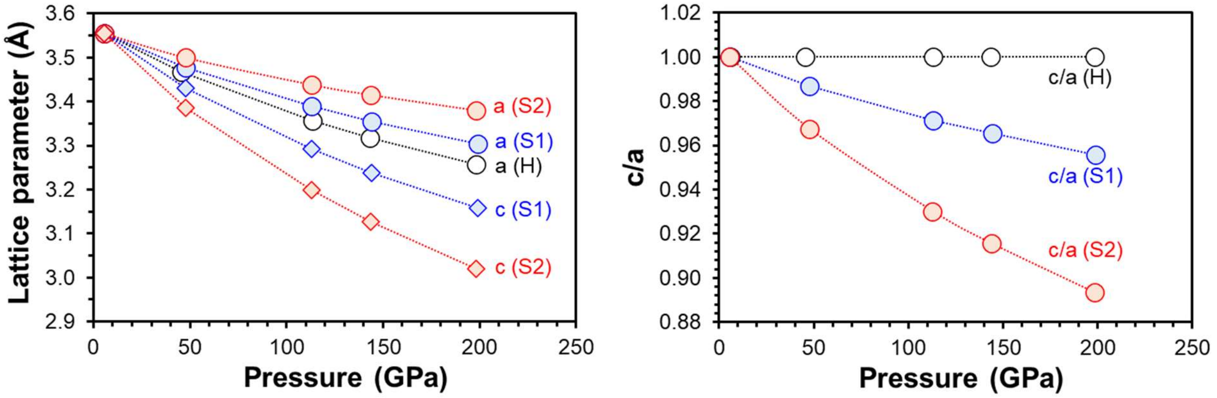

Fig. S5. **Lattice parameters of compressed diamond. Left.** Pressure-induched changes in lattice parameters. H, S1, and S2 refer to hydrostaic compression, uniaxial compression with strain-01, and uniaxial compression with strain-02, respectively. **Right.** c/a of uniaxially compressed diamond.

Figure S6 (Left) shows change in lattic parameter for the compresed diamond with respect to that at 1 atm ($\Delta a/a_0$) where a_0 is lattice parameter at ambient pressure and $\Delta a = a - a_0$. Figure S6 (right) illustrate $\Delta a/\Delta c$ [$(a-a_0)/(c-c_0)$] for diamond under hydrostatic uniaxial compression.

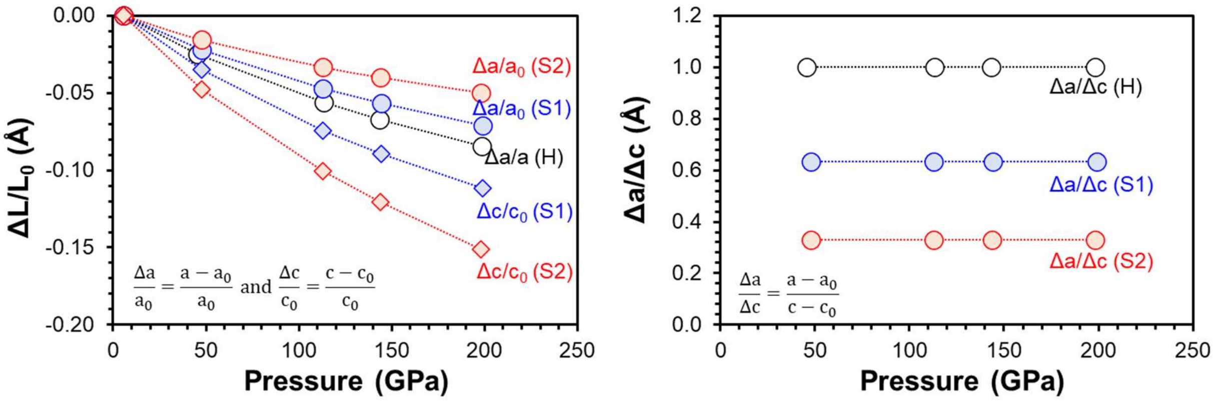

Fig. S6. **Pressure-induced changes in lattice parameter and the ratio of lattice parameters. Left.** Relative change in lattic parameter ($\Delta a/a_0$) for compressed diamond with respect to that at 1 atm, where a_0 refers to the lattice parameter at ambient pressure and $\Delta a = a - a_0$. **Right.** The ratio of the lattice parameter changes in the a- and c-axes of the compressed diamond.

Then, based on Eq. S3 and Eq. S4, strain components ϵ_{11} and ϵ_{33} are estimated;

$$\frac{\Delta a}{a_0} = \epsilon_{11},\ \frac{\Delta c}{c_0} = \epsilon_{33} \tag{S3}$$

$$\frac{\epsilon_{11}}{\epsilon_{33}} = \frac{c_0}{a_0}\frac{\Delta a}{\Delta c} = \frac{\Delta a}{\Delta c} = \frac{a - a_0}{c - c_0}\quad (\because a_0 = c_0) \tag{S4}$$

Finally, figure S7 shows the pressure-induced changs in ϵ_{11} and ϵ_{33} for hydrostatically (H) compressed and uniaxially compressed (S1 & S2) diamond. Tables S3 and S4 shows the pressure-induced changes in the lattice parameters for diamond under hydrostatic and uniaxial compression.

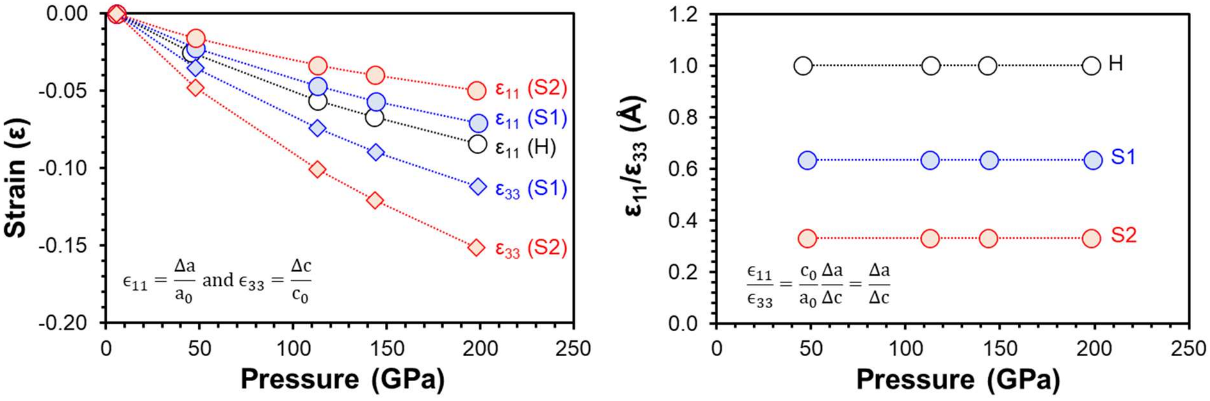

Fig. S7. **Strain and strain ratio [ratio of the changes in the lattice parameters (a-axis and c-axis)] of the compressed diamond.**

Table S3. Strain ratio used for hydrostatically and uniaxially compressed diamond structures.

	Strain	$\varepsilon_{11}/\varepsilon_{33}$
Hydrostatic (H)	$\varepsilon_{11} = \varepsilon_{22} = \varepsilon_{33}$	$\varepsilon_{11}/\varepsilon_{33} = 1.00$
Strain-01 (S1)	$\varepsilon_{11} = \varepsilon_{22}$, $\varepsilon_{33} = 1.58\ \varepsilon_{11}$	$\varepsilon_{11}/\varepsilon_{33} = 0.63$
Strain-02 (S2)	$\varepsilon_{11} = \varepsilon_{22}$, $\varepsilon_{33} = 3.03\ \varepsilon_{11}$	$\varepsilon_{11}/\varepsilon_{33} = 0.33$

Table S4. Lattice parameters of the compressed diamond used to calculate the carbon K-edge IXS spectra and bandgap (E_g) with varying degree of anisotropic compression ($\varepsilon_{11}/\varepsilon_{33} = 1$ for hydrostatic compression; $\varepsilon_{11}/\varepsilon_{33} < 1$ for the uniaxial compression). The pressure values (P) were estimated from the stress tensor: $P = -(\sigma_{11} + \sigma_{22} + \sigma_{33})/3$.

Hydrostatic compression ($\varepsilon_{11}/\varepsilon_{33}$ = 1)					
Pressure (GPa)	a (= b = c) (Å)	V (Å^3)	V/V$_0$	$\varepsilon_{11}/\varepsilon_{33}$	E_g (eV)
5.8	3.5560	44.9661	1.0000	1.00	4.15
45.5	3.4671	41.6773	0.9269		4.32
113.2	3.3569	37.8265	0.8412		4.55
143.4	3.3178	36.5200	0.8122		4.63
198.3	3.2566	34.5361	0.7680		4.77

Uniaxial compression ($\varepsilon_{11}/\varepsilon_{33}$ = 0.63)							
Pressure (GPa)	a (Å)	b (Å)	c (Å)	V (Å^3)	V/V$_0$	$\varepsilon_{11}/\varepsilon_{33}$	E_g (eV)
5.5	3.5560	3.5560	3.5560	44.9661	1.0000	0.63	4.15
47.9	3.4768	3.4768	3.4310	41.4758	0.9224		3.97
112.9	3.3888	3.3888	3.2921	37.8060	0.8408		3.72
144.2	3.3548	3.3548	3.2384	36.4463	0.8105		3.60
198.9	3.3039	3.3039	3.1581	34.4730	0.7666		3.42

Uniaxial compression ($\varepsilon_{11}/\varepsilon_{33}$ = 0.33)							
Pressure (GPa)	a (Å)	b (Å)	c (Å)	V (Å^3)	V/V$_0$	$\varepsilon_{11}/\varepsilon_{33}$	E_g (eV)
5.5	3.5560	3.5560	3.5560	44.9661	1.0000	0.33	4.15
47.9	3.5000	3.5000	3.3860	41.4774	0.9224		3.44
112.8	3.4380	3.4380	3.1980	37.8012	0.8407		2.51
143.8	3.4144	3.4144	3.1264	36.4496	0.8106		2.12
198.2	3.3791	3.3791	3.0191	34.4718	0.7666		1.48

C2. Effect of uniaxial compression on the bandgap of diamond at high pressure

C2.1. Hydrostatic compression.

Figure S8 shows the electronic band structures for hydrostatically compressed diamond ($\varepsilon_{11}/\varepsilon_{33} = 1$) using *ab initio* calculations, which confirms that bandgap (E_g) increases with increasing pressure up to 200 GPa. This increase tends to shift the 1*s* electron excitation energy (i.e., edge-energy onset) of the compressed diamond (see C4 and C5 below for further details).

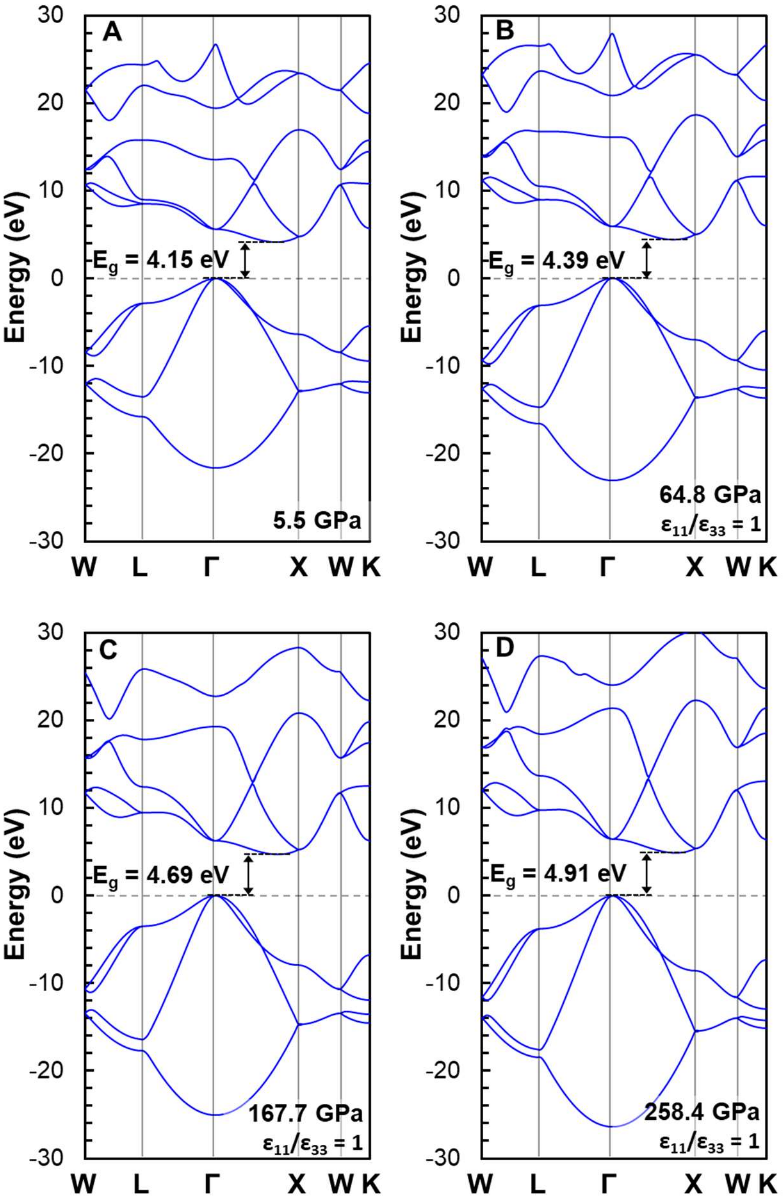

Fig. S8. **Calculated electronic band structures for hydrostatically compressed diamond ($\varepsilon_{11}/\varepsilon_{33}$ = 1).** Band structures are presented along W(0.5, 0.25, 0.75)–L(0.5, 0.5, 0.5)–Γ(0, 0, 0)–X(0.5, 0, 0.5)–W(0.5, 0.25, 0.75)–K(0.375, 0.375, 0.75). Bandgap (E_g) is shown with a black arrow.

C2.2. Uniaxial compression

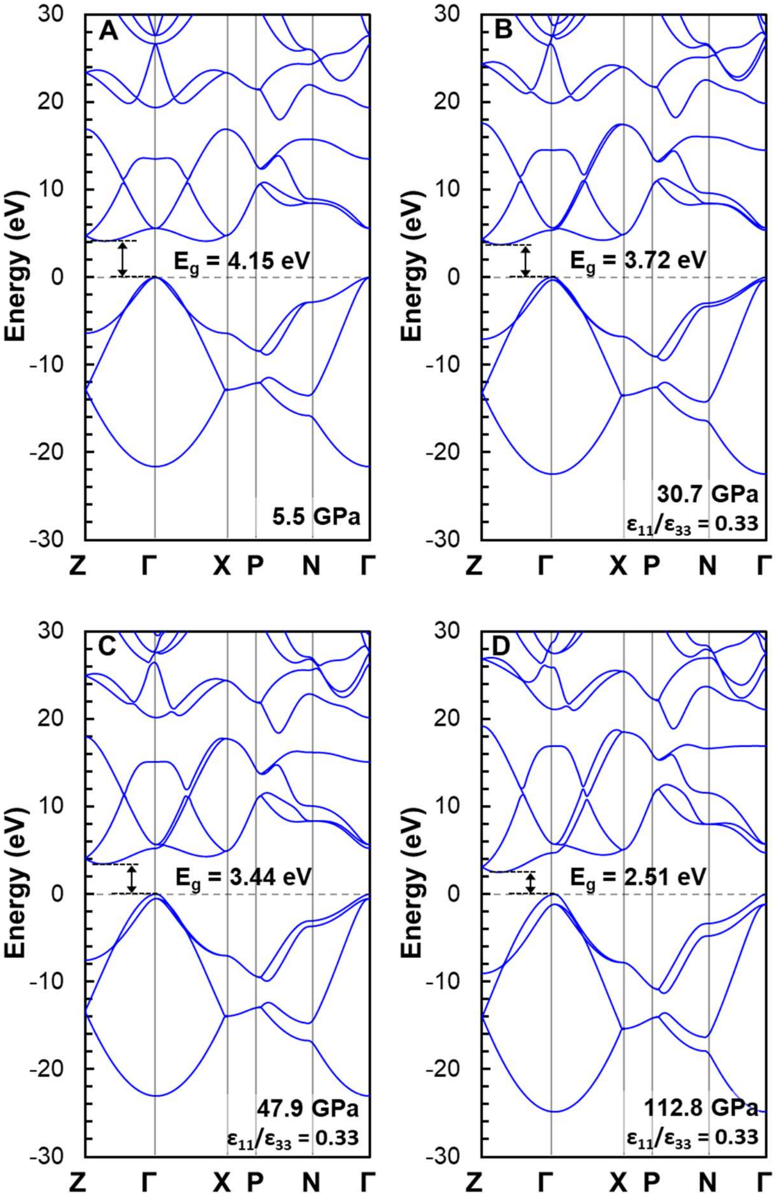

Fig. S9. **Calculated band structures for uniaxially compressed diamond ($\varepsilon_{11}/\varepsilon_{33}$ = 0.33) at high pressure.** The data are presented along Z(0.5, 0.5, −0.5)–Γ(0, 0, 0)–X(0, 0, 0.5)–P(0.25, 0.25, 0.25)–N(0, 0.5, 0)–Γ(0, 0, 0).

Earlier theoretical calculations showed that, if the diamond is compressed uniaxially, its bandgap (E_g) is expected to decrease [e.g., (*60*)]. Our *ab initio* calculations of the compressed diamond are consistent with the pioneering theoretical prediction; the bandgap decreases *gradually* with increasing pressure, and the degree of the decrease depends on the degree of uniaxial compression. This decrease is in contrast to those observed in hydrostatically compressed diamond, where the systematic increase in the bandgap is observed (Figures S8 and S9).

Figure S10-A shows the effect of pressure and the degree of anisotropy on the bandgap (E_g) of the compressed diamond. Figure S10-B reveals the pressure gradient of the bandgap (i.e., dE_g / dP). While E_g of the isotropically compressed diamond increases *gradually* with increasing pressure, with a positive dE_g/dP value of 0.0030, the gradients for $\varepsilon_{11}/\varepsilon_{33}$ = 0.63 (dE_g/dP = −0.0038) and for $\varepsilon_{11}/\varepsilon_{33}$ = 0.33 (dE_g/dP = −0.0139) are negative. This result indicates that an increase in anisotropy further decreases E_g for the compressed diamond (Table S5).

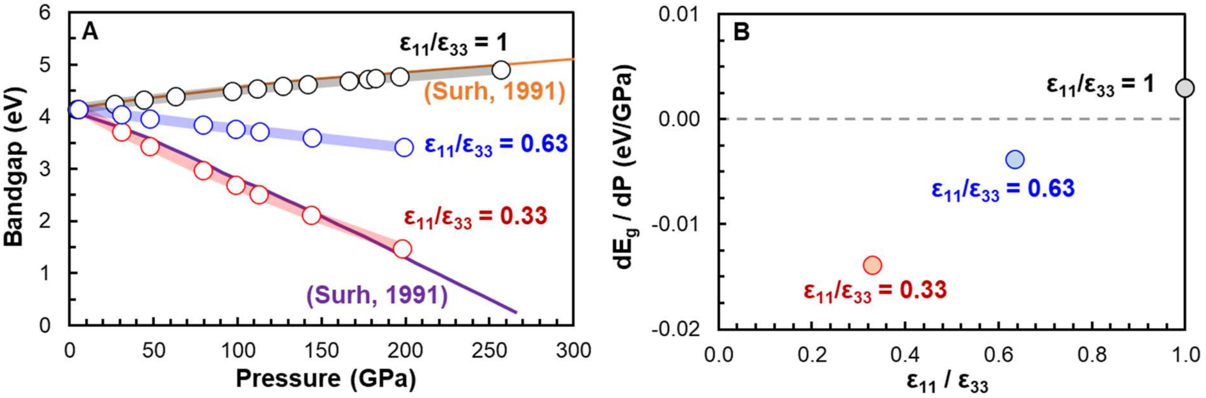

Fig. S10. **Effect of pressure on the bandgap (E_g) of diamond with varying anisotropic strain.** (**A**) Variations in the E_g with varying degrees of anisotropic compression; $\varepsilon_{11}/\varepsilon_{33}$ = 1 for the hydrostatic compression; $\varepsilon_{11}/\varepsilon_{33} < 1$ for the uniaxial compression. (**B**) Variations in dE_g/dP with varying $\varepsilon_{11}/\varepsilon_{33}$, as labeled.

Table S5. The effect of pressure on the bandgap (E_g) from the calculated band structures for the compressed diamond with varied strain ratio ($\varepsilon_{11}/\varepsilon_{33}$).

Strain ratio	Bandgap (E_g; eV) *vs.* Pressure (*P*; GPa)
$\varepsilon_{11}/\varepsilon_{33}$ = 1.00	$E_g = 0.0030\times P + 4.19$ (R^2 = 0.9875)
$\varepsilon_{11}/\varepsilon_{33}$ = 0.63	$E_g = -0.0038\times P + 4.16$ (R^2 = 0.9981)
$\varepsilon_{11}/\varepsilon_{33}$ = 0.33	$E_g = -0.0139\times P + 4.13$ (R^2 = 0.9943)

C3. Effect of anisotropic compression on C-C bond distance in compressed diamond.

Figure S11 shows the lattice structures of diamond under compression at ~ 200 GPa with varying degrees of anisotropic compression. Regardless of the type of compression (both hydrostatic and uniaxial), the C-C bond length decreases with increasing pressure. In addition, the interatomic distance between the second NN carbon atoms diverges upon uniaxial compression (Figure S12).

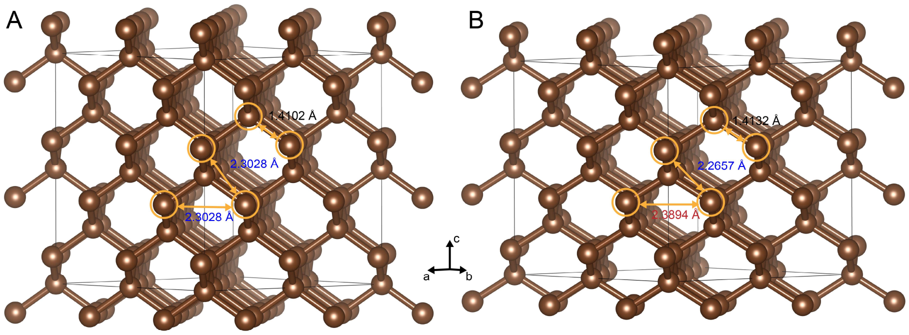

Hydrostatic compression, ~200 GPa ($\varepsilon_{11}/\varepsilon_{33}$ = 1.0)

Uniaxial compression, ~200 GPa ($\varepsilon_{11}/\varepsilon_{33}$ = 0.33)

Fig. S11. **Lattice structures of diamond under compression at ~ 200 GPa with varying degrees of anisotropic compression with $\varepsilon_{11}/\varepsilon_{33}$ = 1 (hydrostatic) and $\varepsilon_{11}/\varepsilon_{33}$ = 0.33 (uniaxial).** The interatomic distances between the first-order (1.4132 Å; black) and second-order (2.2657 and 2.3894 Å; blue and red, respectively) nearest-neighbor carbon atoms are shown.

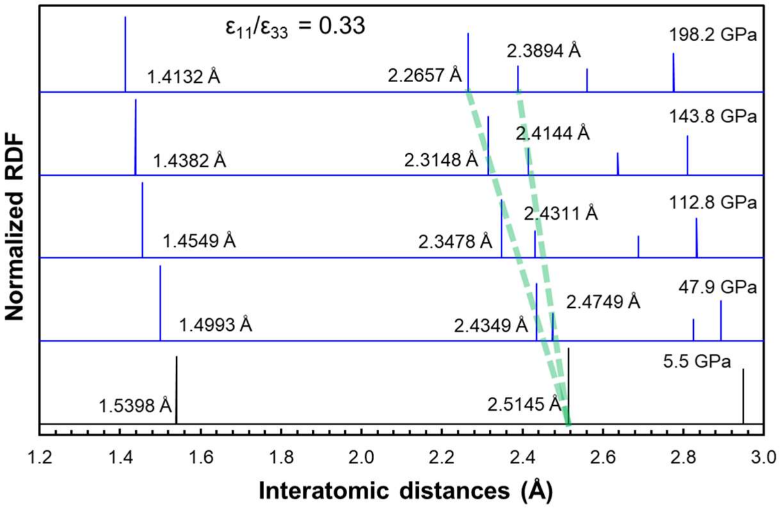

Fig. S12. **Normalized radial distribution functions for the uniaxially compressed diamond ($\varepsilon_{11}/\varepsilon_{33}$ = 0.33) with varying pressure.**

At constant pressure, Figures S13 and S14 reveal that the next-nearest C-C bond distance noticeably changes and bifurcates with increasing degree of anisotropy. However, the nearest C-C bond length does not change with varying degrees of anisotropic compression.

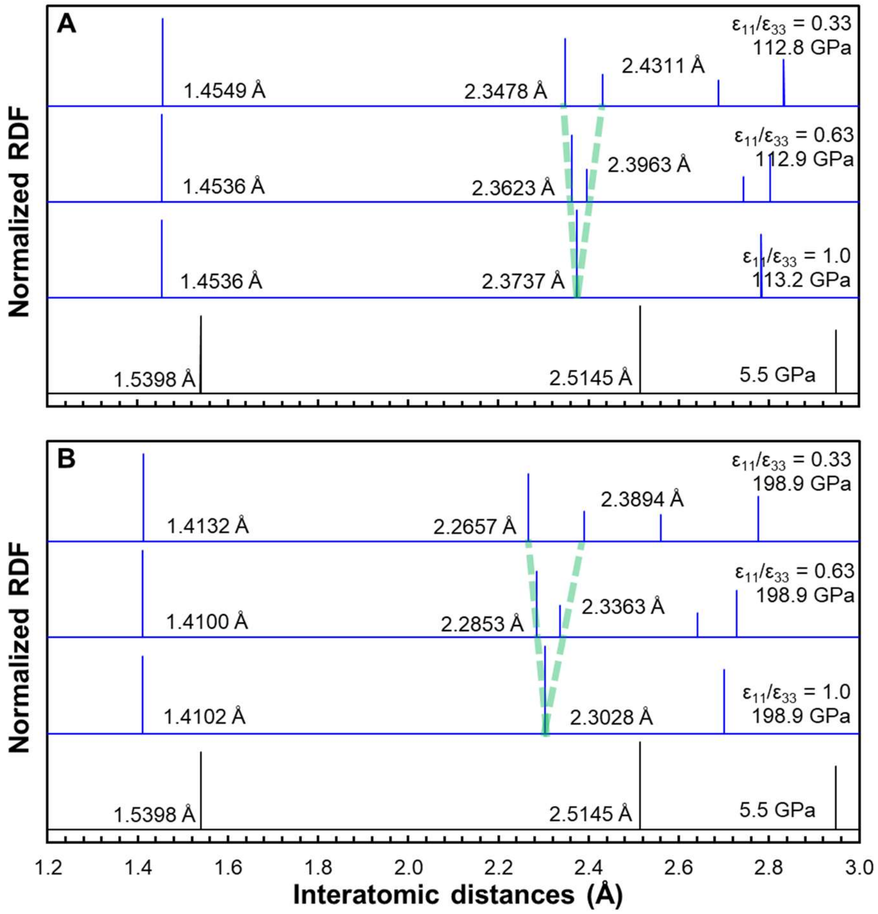

Fig. S13. **Normalized C-C bond distance distribution for compressed diamond under compression.** (**A**) at ~113 GPa and (**B**) and ~200 GPa with varying strain ratio ($\varepsilon_{11}/\varepsilon_{33}$ = 1.0, 0.63, and 0.33), as labeled.

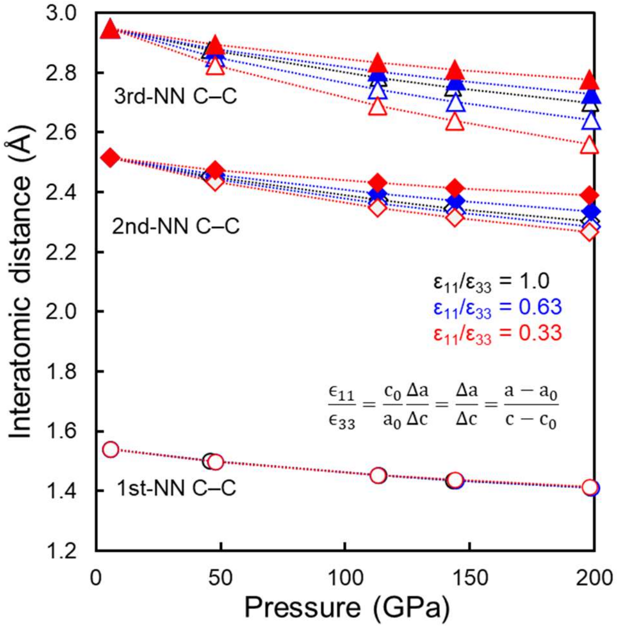

Fig. S14. **Variation in the interatomic distance between the first-order (first-NN), second-order (second-NN), and third-order (third-NN) nearest-neighbor carbons with varying pressure and the strain ratio ($\varepsilon_{11}/\varepsilon_{33}$), as labeled.** The C-C distance based on hydrostatic compression ($\varepsilon_{11}/\varepsilon_{33} = 1.0$) is shown in black; uniaxial compression with $\varepsilon_{11}/\varepsilon_{33} = 0.63$ and with $\varepsilon_{11}/\varepsilon_{33} = 0.33$ are shown in blue and red, respectively.

C4. Effect of uniaxial compression on the IXS patterns of compressed diamond at high pressure (hydrostatic *vs.* uniaxial compression)

C4.1. IXS spectral pattern.

We performed *ab initio* calculations of IXS spectra for uniaxially compressed diamond with pressures up to 2 Mbar. Figures S15 and S16 (top) show the calculated carbon K-edge IXS spectra for diamond under compression, with strain ratios ($\varepsilon_{11}/\varepsilon_{33}$) from 1 (hydrostatic) to 0.33 (uniaxial compression). Figure S16 shows the changes in the calculated positions of the IXS patterns with pressure and the varying degree of anisotropy. The peak positions for E_0 and P1 of the IXS patterns for the diamond somewhat vary with varying degree of anisotropic compression (See sections C4.2 and C4.3 for details). However, regardless of the degree of anisotropic compression, the peak positions for E* and other high energy peaks are not substantially affected. In particular, the calculated results reveal that the E* position does not vary noticeably with varying degrees of anisotropic compression (Figures S10-S12).

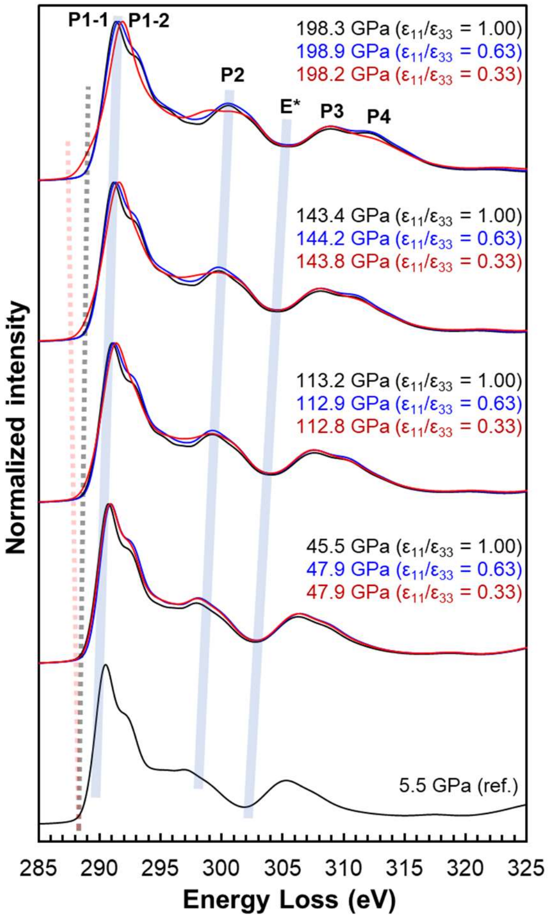

Fig. S15. **Calculated carbon K-edge IXS spectra for diamond under compression with varying strain ratios ($\varepsilon_{11}/\varepsilon_{33}$) from 1 to 0.33.** The pressure values were estimated from the stress tensor: $P = -(\sigma_{11} + \sigma_{22} + \sigma_{33})/3$. Gaussian broadening (FWHM) of 0.5 eV is used to mimic instrumental broadening.

Hydrostatic *vs.* Uniaxial compression

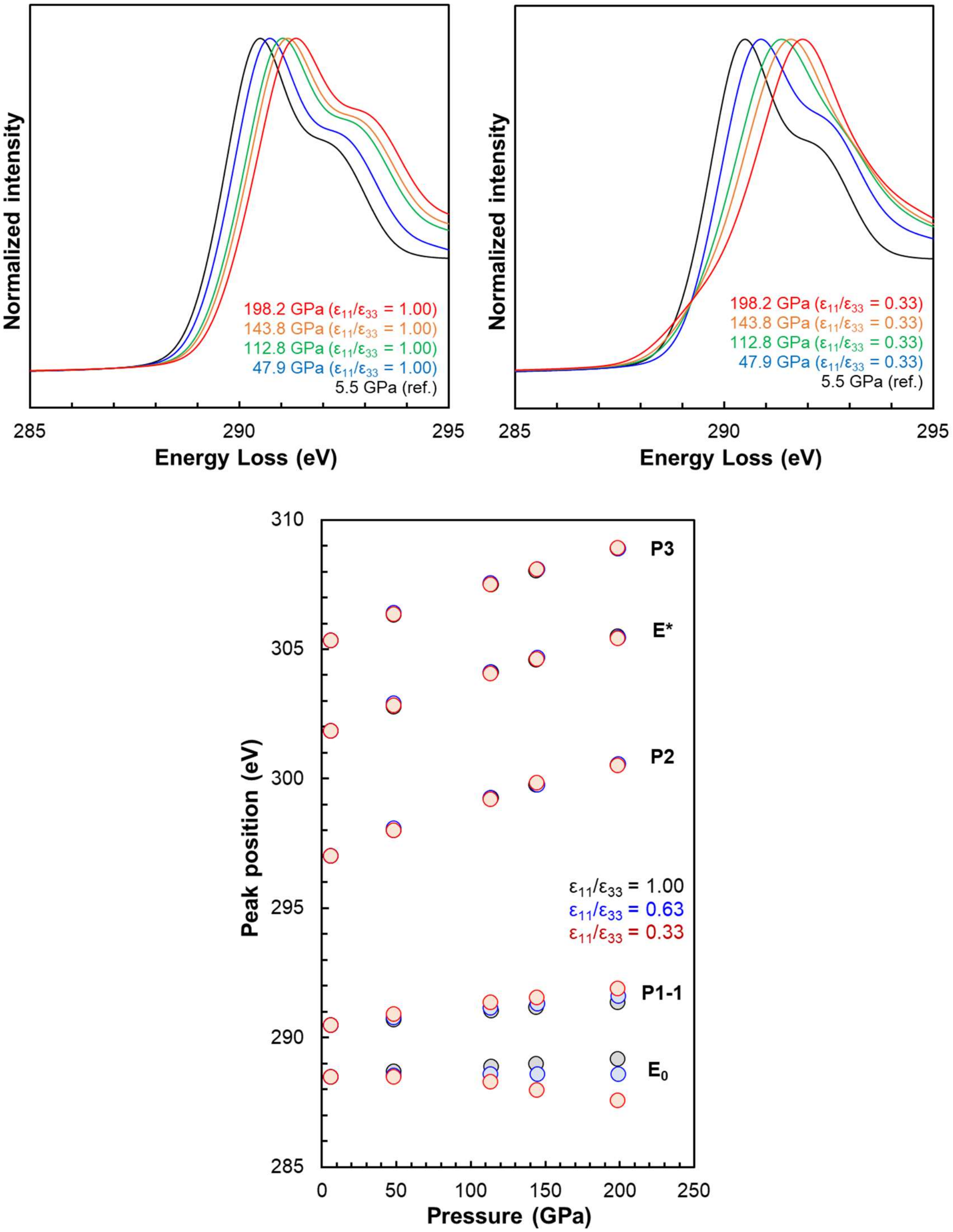

Fig. S16. **Effect of pressure on carbon K-edge IXS features of diamond under hydrostatic and uniaxial compression. Top.** Calculated carbon K-edge IXS features of diamond under hydrostatic (Left, $\varepsilon_{11}/\varepsilon_{33}$ = 1) and uniaxial compression (Right, $\varepsilon_{11}/\varepsilon_{33}$ = 0.33). **Bottom.** Effect of pressure on the IXS peak positions.

Table S6 shows the pressure-induced changes in P1-1 peak position in our calculated IXS spectra for the compressed diamond, revealing a linear relationship between pressure and IXS peak position. With increasing anisotropy, the pressure-induced changes in peak position become more prevalent, as is evident from Figure S16. The results with positive value (i.e., shift /pressure) confirm the gradual increase in electronic excitation energy in compressed diamond with pressure.

Table S6. The linear relationships between P1-1 peak positions in the calculated IXS spectra for compressed diamond *vs.* pressure with varying strain ratio ($\varepsilon_{11}/\varepsilon_{33}$) obtained from *ab initio* calculations.

Strain ratio	Peak position of P1-1 (eV) vs. Pressure (P; GPa)
$\varepsilon_{11}/\varepsilon_{33} = 1$	P1-1 = $0.0046 \times P + 290.5$ ($R^2 = 0.990$)
$\varepsilon_{11}/\varepsilon_{33} = 0.63$	P1-1 = $0.0058 \times P + 290.5$ ($R^2 = 0.998$)
$\varepsilon_{11}/\varepsilon_{33} = 0.33$	P1-1 = $0.0072 \times P + 290.5$ ($R^2 = 0.992$)

C4.2. Estimation of edge-energy onset.

The IXS pattern reveals a pressure-induced change in edge-onset that yields spectral patterns of the uniaxially compressed diamond, a change that is distinct from that which occurs under hydrostatic compression at high pressure (Figure S17): Upon hydrostatic compression, the edge energy (E_0) in the C K-edge IXS spectrum of compressed diamond increases with increasing pressure, while upon uniaxial compression, the edge-energy onset tends to decrease slightly with pressure, and the detailed trends depend on the degree to which the crystal is uniaxially compressed (Figures S17-S18, and Figure S19). Figure S16 also shows that edge energy shifts to lower energy with an increasing degree of anisotropic strain.

The resolution of ~0.02 eV in the simulated spectrum for the compressed diamond can be useful for estimating the true edge-onset and, therefore, the band-gap (Figure S17). However, given the current spectral resolution and the signal-to-noise ratio of the experimental IXS pattern, it is not trivial to locate the edge-energy onset (E_0) from the IXS spectra themselves, as locating the position of the non-zero spectral build-up is subject to uncertainty. Here, we obtained E_0 using the protocols described in Figure S18. First, the baseline is identified. Then a linear line is drawn from the near-edge spectral pattern. The E_0 is then determined from the energy position where the two lines intersect, so the peak position of the edge-energy onset is expected to be higher than the true E_0.

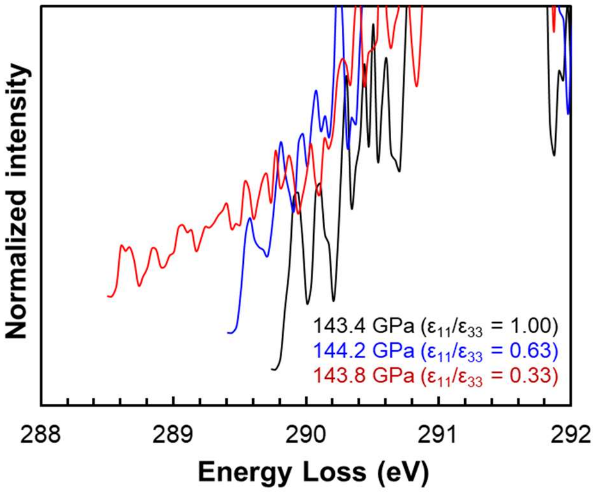

Fig. S17. Carbon K-edge IXS features of diamond under uniaxial compression at a pressure of ~140 GPa near the absorption edge at ~290 eV. Various strain ratios ($\varepsilon_{11}/\varepsilon_{33}$) were applied to the diamond structures to establish how the anisotropic stress affects diamond's electronic structures. The broadening factor of 0.02 eV was used to show the onset of IXS features.

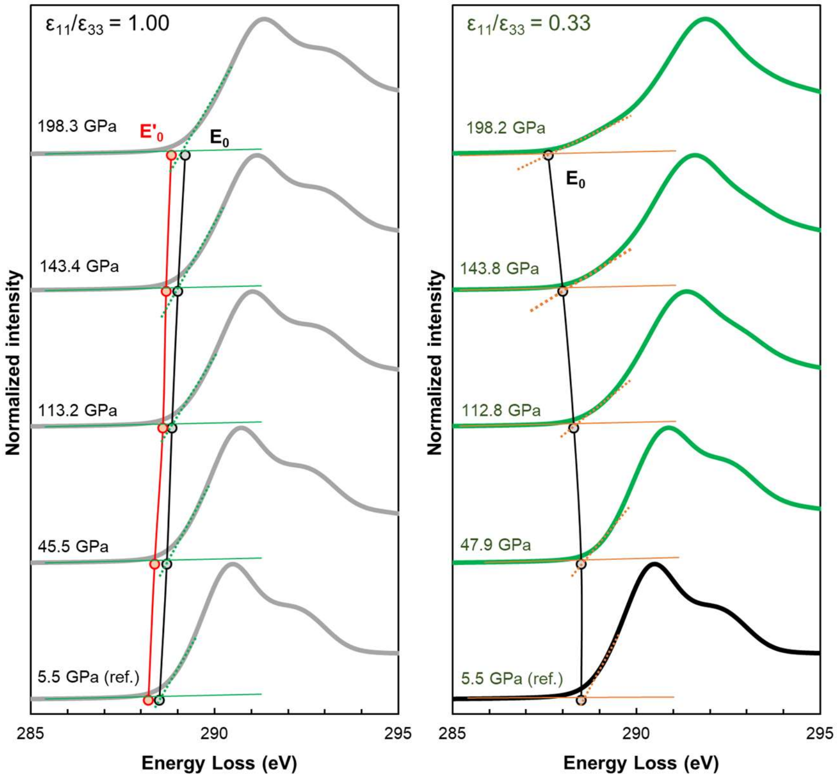

Fig. S18. **Protocols used to determine the E_0 values for the calculated carbon K-edge IXS spectra of the compressed diamond with varying strain ratios, as labeled.**

The pressure-induced increase in the bandgap in oxide materials is often accompanied by an increase in edge-energy onset (*28*). While these results highlight that the IXS E_0 pattern can be used to infer the change in the bandgap of the compressed diamond, the direct estimation of the optical bandgap (that could also result from a minute change in DOS) from the edge-energy onset (that is mainly effective in estimating a *moderate* change in average DOS) is not trivial: as spectral intensity near the energy-edge onset is small, identifying the build-up of spectral intensity directly from the IXS spectrum is difficult, and care must be taken to provide fully quantitative estimation of the bandgap using the protocol. The inference to be taken here is a semi-qualitative trend in the bandgap of diamond under compression (see C6 below). Having said that, the E_0 can be rather easily estimated from the experimental IXS spectra and is practically useful to infer the pressure-induced changes in population of average electronic density of states. Therefore, in the current manuscript, we discuss the evolution of E_0 with pressure.

C4.3. Effect of pressure and uniaxial compression on peak positions in IXS spectra for diamond at high pressure.

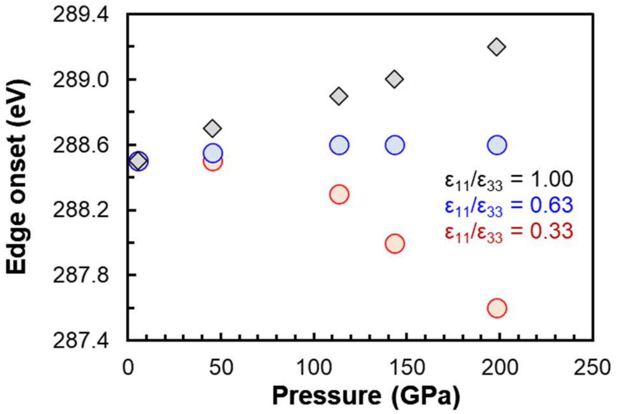

Fig. S19. Pressure dependence of the edge-energy onset with varying strain ratios ($\varepsilon_{11}/\varepsilon_{33}$), as labeled.

C5. Effect of scattering geometry on the IXS patterns of compressed diamond at high pressure (scattering vector parallel to the compression axis *vs.* scattering vector perpendicular to the compression axis)

C5.1. *Ab initio* calculations.

The C K-edge IXS spectra of the compressed diamonds were calculated with varying strain ratios [$\varepsilon_{11}/\varepsilon_{33}$ = 1 (hydrostatic) and 0.33] and scattering geometry using the full-potential linearized augmented plane wave with local orbitals (FP-LAPW+lo) method (Wien2K) (*57*) and the Perdew-Burke-Ernzerhof exchange-correlation functional. The Muffin-Tin radius of carbon of 1.2 a.u. was used, allowing us to avoid core overlap in the compressed diamond. The energy for core–valence separation of −6.0 Ry, and the 6×6×6 Monkhorst-Pack grid (total of 108 *k* points) were used. The convergence of self-consistent field calculations was met with 1×10^{-4} Ry and 1×10^{-3} e for the total energy and charge distance, respectively. Inelastic scattering of incident X-rays involves the electronic transition of 1*s* electron to the unoccupied states. The ELENES module implemented in the Wien2K code enables calculations of such transitions from the transition matrix of double differential scattering cross section, consisting of dynamic structure factor (*57*). The C K-edge IXS spectra of the compressed diamonds were calculated with varying strain ratios [$\varepsilon_{11}/\varepsilon_{33}$ = 1 (hydrostatic) and 0.33] and scattering geometry using the full-potential linearized augmented plane wave with local orbitals (FP-LAPW+lo) method (Wien2K) (*57*) and the Perdew-Burke-Ernzerhof exchange-correlation functional. Finally, the crystal-orientation-dependent carbon K-edge IXS spectra were calculated to explore the effect of scattering geometry ($q \perp \mathrm{c}$ and $q \parallel c$) on IXS spectral patterns. Here, *q* and *c* refer to the scattering vector and [001] the direction, respectively. The scattering geometry of $q \perp \mathrm{c}$ and $q \parallel c$ can be described with the Euler angles of (0°, 0°, 0°) and (0°, 90°, 0°), respectively. The scattering geometry-dependent carbon K-edge spectra for graphite calculated in the current study are consistent with the results reported in a previous study (Figure S20) (*62*). In ELENES module, the *q*-vector range can be defined using the detector collection semi-angle and the microscope collection semi-angle (*57*). These were set to 5.0 and 1.87 mrad (0.29° and 0.11°) for the low-q limit, therefore selectively observing dipole-allowed transitions only. The pressure (*P*) was estimated from the stress tensor: $P = -(\sigma_{11} + \sigma_{22} + \sigma_{33})/3$.

C5.2. IXS patterns for compressed diamond with varying scattering geometry (scattering vector perpendicular to compression axis *vs.* parallel to compression axis) on C K-edge IXS spectra for compressed diamond at high pressure.

The dynamic structure factor [S(q)] of compressed diamond contains information about the electronic structure along the direction of the scattering vector (q). Therefore, depending on the orientation [perpendicular ($q \perp c$) *vs.* parallel ($q \parallel c$) to the compression axis [001]] of the diamond anvil relative to incoming x-ray, distinct electronic structures are probed, resulting in different IXS spectra. Orientation-driven changes in the C K-edge IXS patterns have been reported for graphite under pressure (*21*) and at ambient conditions (*62*), and similar orientation dependence has been reported in earlier IXS studies for uniaxially compressed BN (*63*). Here, C K-edge IXS spectrum of graphite is calculated with varying scattering geometry, demonstrating the spectral pattern's distinct crystal-orientation dependence (Figure S20). The result is consistent with the earlier experimental and theoretical results (*21, 62*).

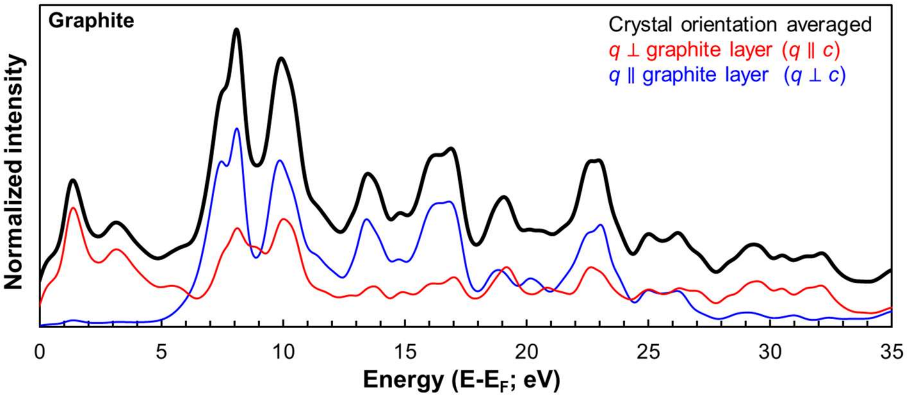

Fig. S20. **Calculated carbon K-edge IXS spectra for the graphite.** Crystal orientation average (black); scattering vector (q) perpendicular to the compression axis ([001]) (blue, $q \perp c$); scattering vector parallel to the compression axis (red, $q \parallel c$).

To identify further the effect of scattering geometry on the DOS for uniaxially compressed diamond, we calculated the IXS spectra with varying crystal orientation. Figure S21 shows the C K-edge IXS spectra for uniaxially compressed diamond with varying scattering geometry. The result reveals that the edge-onset energy of the uniaxially compressed diamond with $q \perp c$ can also increase with pressure. In contrast, the edge energy of calculated IXS spectrum projected along the $q \parallel c$ direction to the compression axis tends to decrease with increasing pressure (Figure S21-right). Therefore, the edge energy for the diamond with $q \perp c$ geometry is systematically larger than that with $q \parallel c$. The results also reveal that the pressure-induced change in the E* position is negligible, so it can be used as a pressure indicator.

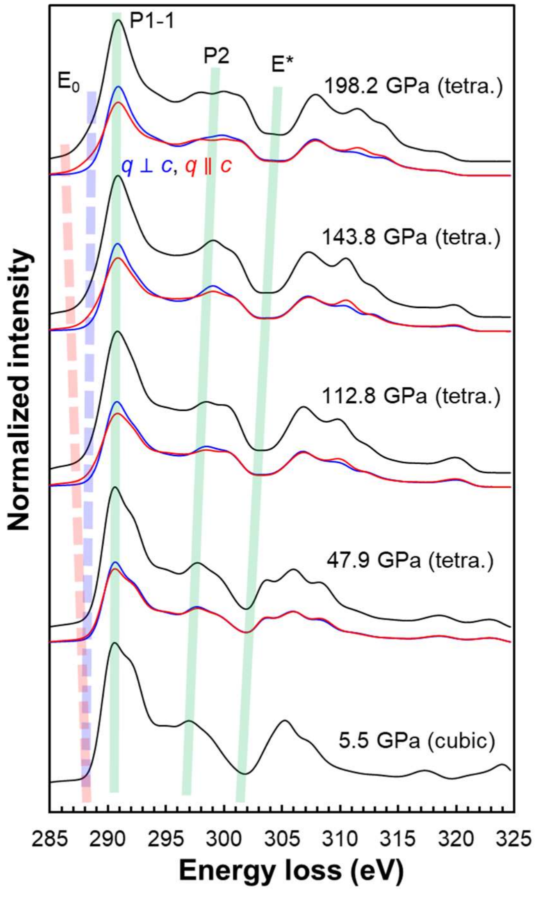

Fig. S21. **Calculated carbon K-edge IXS spectra for uniaxially compressed diamond with $\varepsilon_{11}/\varepsilon_{33}$ = 0.33.** Crystal-orientation-averaged K-edge spectrum (black) is shown with K-edge spectrum with two distinct scattering geometries [$q \perp c$ (blue) and $q \parallel c$ (red)].

Figure S22 shows the pressure dependencies of the characteristic peak positions in the calculated carbon K-edge IXS patterns of the compressed diamond structures with varying strain ratios. Figure S22-B shows the pressure-induced changes in the IXS peak positions (E*, E_0, and P1) of the uniaxially compressed diamond with varying C-C bond lengths, confirming that E* can be used to infer the nearest C-C bond length in compressed diamond.

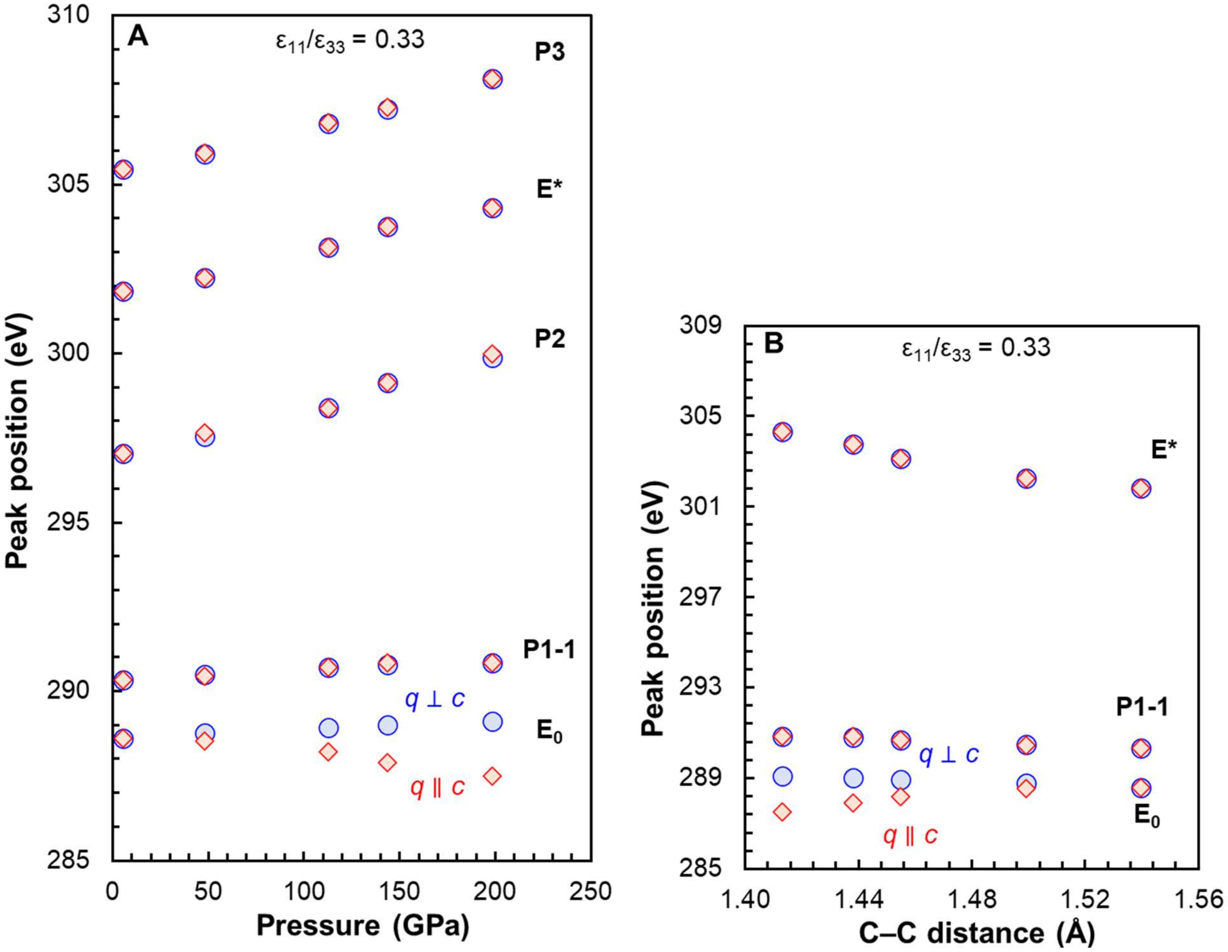

Fig. S22. Variations of the characteristic peak positions in carbon K-edge IXS spectrum for uniaxially compressed diamond ($\varepsilon_{11}/\varepsilon_{33}$ = 0.33) with varying scattering geometry [*q* ⊥ *c* (blue) and *q* ∥ *c* (red)]. (**A**) Effect of pressures. (**B**) The relationship between peak positions and interatomic distances between nearest-neighboring C–C bond length.

C6. Comparion with experimental IXS spectra for compressed diamond at high pressure

As shown in Figure S1, the diamond is under uniaxial compression. The scattering geometry of the current experiment selectively probes the electronic structure (DOS) perpendicular to the compression direction ([001], $q \perp c$), so a comparison between the experimental result and the theoretically calculated IXS spectrum for uniaxially compressed diamond with $q \perp c$ geometry can be made.

As discussed in section C5, a moderate degree of uniaxial compression results in a decrease in the edge-energy onset. This is certainly opposite to the observed trend in the experimental IXS spectra where the peak position of the edge-onset positively shifts with increasing pressure (Figure 1). The observed increase in the experimental IXS patterns may be seen as if the diamond would be under hydrostatic compression. However, our experimental data with increasing edge-energy onset are not fully consistent with the trend under hydrostatic compression, as they are somewhat smaller than those predicted for hydrostatic compression (Figure S23). While the change in edge energy is small, the slight discrepancy between the experimental data and theoretical results based on hydrostatic compression can be attributed mainly to the uniaxial compression of the diamond. Specifically, as shown in section C5, the calculated edge-energy onset for the IXS spectra for the uniaxially compressed diamond with $q \perp c$ geometry also increases with increasing pressure, yet the change is smaller than the changes under hydrostatic compression (Figure S23-right). The calculated trend with $q \perp c$ geometry shows similarity with the experimental trend, indicating that the experimental IXS spectrum is primarily attributed to changes in electronic density of states under moderate uniaxial compression with primarily $q \perp c$ scattering geometry. Therefore, based on the *ab initio* results and comparing them with experimental data, the current experimental IXS spectrum of the compressed diamond reports primarily pressure-induced changes in DOS perpendicular to the compression axis. Figures 1 and 2 in the main text have been drawn to reflect this point.

Figure S23 also shows that the edge-energy onset (E_0) and the bandgap (E_g) are not identical, while the trend can be rather consistent (see C4.2 above). We finally note that it is beyond the scope of the current manuscript to estimate the exact value $\varepsilon_{11}/\varepsilon_{33}$ (our ongoing *ab initio* study will delve farther into quantifying the degree of uniaxial compression). Nonetheless, the observed similarilty incidates that $\varepsilon_{11}/\varepsilon_{33}$ may not be notably different from the value (of 0.33) used in the currenty theoretical study.

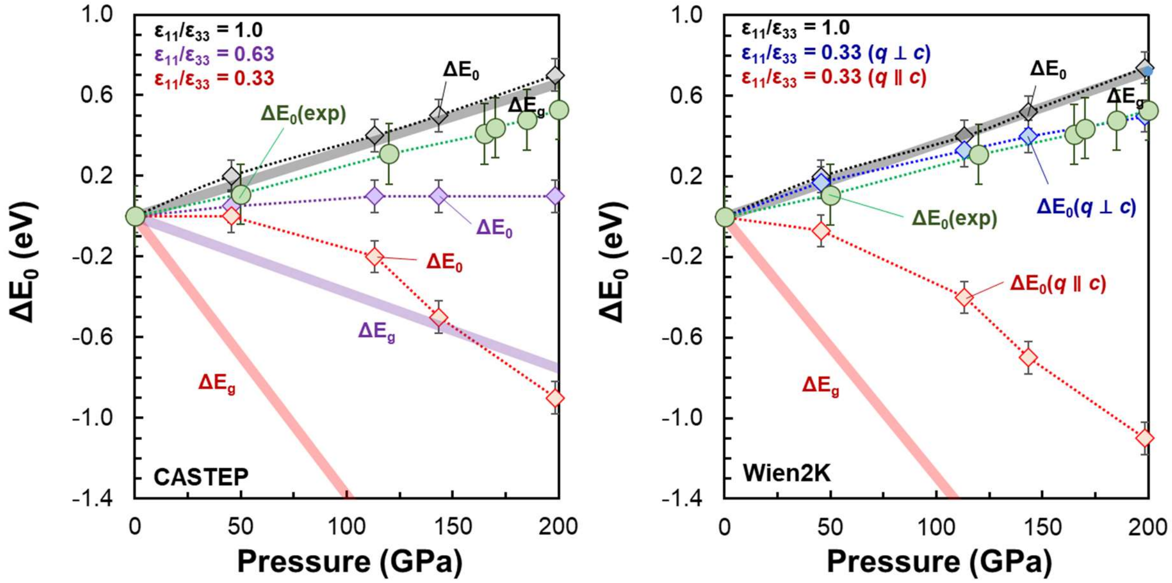

Fig. S23. **Pressure-induced changes in the IXS spectral pattern for hydrostatically and uniaxially compressed diamond. Left.** Pressure-induced changes in the edge-energy onset, ΔE_0 and ΔE_g of the IXS spectra for hydrostatically and uniaxially compressed diamond. **Right.** Pressure-induced changes in the edge-energy onset, ΔE_0 and ΔE_g for unxiasially compressed diamond ($\varepsilon_{11}/\varepsilon_{33}$) with $q \perp c$ and $q \parallel c$ geometry.

D. Effect of pressure on bulk moduli and IXS spectral spectral patterns for compressed diamond and crystalline oxides at high pressure

Figure S24 shows the changes in edge-energy onset E_0, E*, and E_C of the IXS spectra hydrostatically compressed diamond and oxide phases at high pressure as labeled. As we are concerned about the bulk modulus of the *istropically* compressed materials, all the IXS spectral patterns are from the isotropically compressed diamond and oxides. While an increase in E_C is mainly due to an increase in E_0 for other softer oxides, E_0 for the hydrostatically compressed diamond does not vary much with pressure and an increase in E_c and E* for the compressed diamond mostly stems from the electronic dispersion in DOS.

The bulk modulus of $MgSiO_3$-bridgmanite increases with increasing pressure from 356 (at ~25 GPa) to 698 GPa (at ~120 GPa); those for SiO_2 phases also range from ~316 GPa (at 9 GPa, stishovite) to ~324 GPa (at ~120 GPa, PbO_2-type) [see (*64-68*) and references therein]. These are much smaller than those of diamond under compression with its bulk modulus ranging from 466 (at ~6 GPa) to 825 GPa (at ~113 GPa) (*38*).

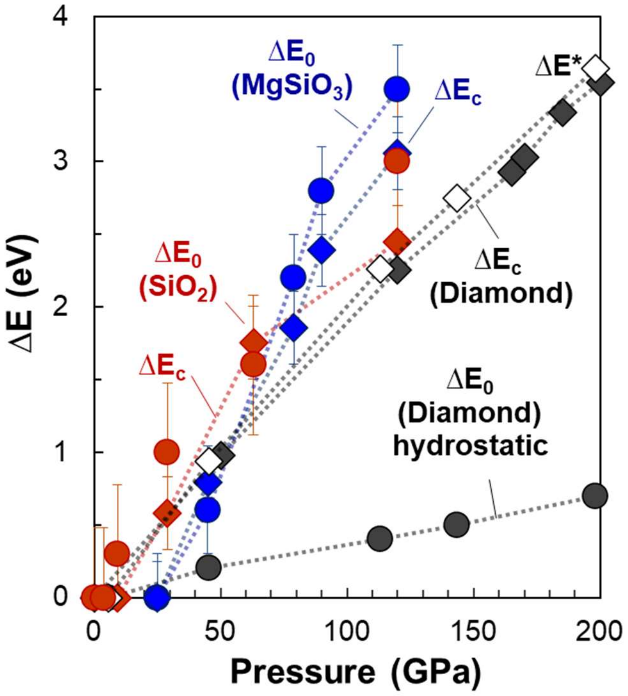

Fig. S24. **Pressure-induced changes in edge-energy onset, E*, and E_C of the IXS spectra for hydrostatically compressed diamond, SiO_2, and $MgSiO_3$ phases with respect to those at 1atm**. See (*24*, *28*, *30*) for the original data.

E. Relationship between hardness, bulk modulus, and electronic DOS in diamond

E1. Hardness *vs.* bulk modulus

Hardness is a measure of material's resistance to deform under indentation. It depends on both intrinsic (crystal structure, chemical bond, and electronic structures) and extrinsic (e.g., defects and large-scale imperfections in crystals) factors. Bulk modulus is a measure of incompressibility of a material. Bulk modulus of super-hard materials with exceptional incompressibility has shown strong correlation with the bulk hardness as both properties mainly record response to external indentation (*41, 69*), while the discrepancy between these properties increase for the less hard materials.

Earlier macroscopic (empirical) and microscopic theoretical models provided insights into relationship between intrinsic chemical hardness and bulk modulus (*20, 40-45, 70-73*). These are based on calculations of the bulk modulus and convert it into the known correlations between the hardness and bulk modulus [e.g., (*41, 69*) and references therein]. While it is not trivial to establish a link between bulk modulus and hardness of multi-component super-hard materials, relationship for single component diamond is much less complicated and primarily depend on the nature of C-C bond. Chemical (intrinsic) hardness of covalent crystal corresponds positively with its bulk modulus [e.g., (*40-44, 71, 72*) and references therein]. Taking these into consideration, while our discussion is mainly centered around bulk modulus, yet it can also be extended to account for the material's hardness.

E2. Bulk modulus, bond properties, and electronic structures

Earlier pioneering efforts presented empirical and *ab initio* based models that established a link between material hardness, incompressibility, and characteristics of bond; hardness has been linked to strength of chemical bond that has been parameterized with various bond properties. Particularly, material's hardness tends to increase with, shorter bond length, higher electronic density, and enhanced covalence in bond [see (*39, 41, 45, 70, 71, 73, 74*) and references therein]. Furthermore, hardness is reported to correlate well with bond density (the number of covalent bond/volume) (*75*), electronegativity of bond (*71*) its iconicity of bond, not to mention overall crystal structures (*71, 73, 74, 76*); energy gap (or bandgap) of materials can often be used to account for the hardness (*39, 70*). Bulk modulus increases with an increase in Mulliken overlap populations (*45, 70*). Detailed overview of the microscopic models of hardness and incompressibility can be found elsewhere [see (*40-44, 70*) and references therein].

As for the effect of pressure on hardness and bulk modulus, earlier studies have shown that hardness at high pressure is directly calculated from the bulk modulus, sharing identical pressure dependence (*42, 72*). Theoretical studies showed that hardness of covalent bonds in diamond increases with increasing pressure (*76*). Currently, the experimental estimation of diamond's elastic constants and properties have been limited up to ~19 GPa (*2*).

E3. Bulk modulus and DOS of compressed diamond

All the aforementioned bond properties, such as energy gap, and orbital overlap populations have direct correspondences to how unoccupied electronic DOS (as proved by IXS) evolves under compression, as DOS results from collective electronic interactions and the nature of bond. Particularly, full DOS of diamond contains complex information of overlap integrals of atomic orbitals that are closely related to the bond strength of diamond. The pressure-driven changes in bond properties of materials including Mulliken overlap population (MOP) under compression are well manifested in changes in DOS patterns with pressure. In this study, IXS provides a direct access to the DOS of compressed diamond beyond multi-megabar pressures experimentally. We established a direct link between C-C bond length, MOP and E*(Figures 1 and 2). Similar relationship can be established for bulk modulus (Figure 2 E-F).

E4. Effect of pressure on bulk modulus and DOS of compressed diamond

Pressure-induced electronic dispersion *vs.* ΔE* (2nd band gap energy at high pressure – that at 1 atm). Electronic dispersion of the compressed diamond is demonstrated in Figure S25; here, to quantify the pressure-induced dispersion, the peak position difference in P4 and P1 (Figure 1B) has been used as a measure of peak width and the degree of electronic dispersion in DOS. Figure S25 shows the relationship between such peak width [normalized with respect to that at 1 atm, peak position difference (P4-P1) at high pressure – that at 1 atm] and ΔE*, confirming that ΔE* effectively parameterizes the pressure-induced peak width (an increase in electronic dispersion in electronic 1*s* excitation) in the unoccupied DOS spectra of diamond at high pressure.

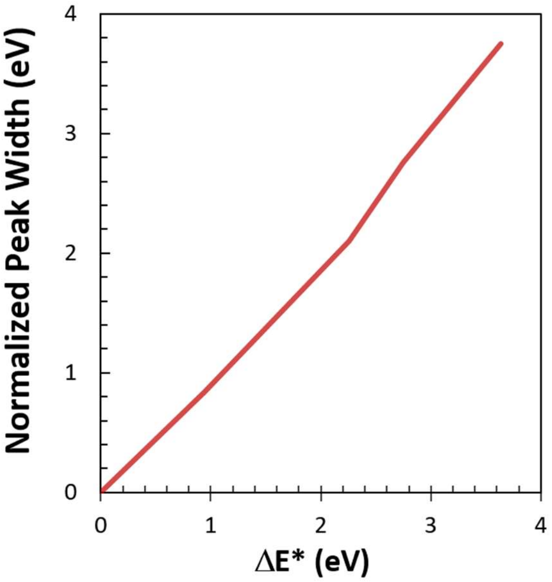

Fig. S25. **Relationship between ΔE* and peak width defined as peak position difference (P4-P1, Figure 1).** The width of the IXS pattern is further normalized with respect to that at 1 atm.

Bulk modulus *vs.* ΔE* in diamond. Figure S26 reveals positive correlation between bulk modulus (*38*), Vickers hardness of diamond under compression (*72*), and ΔE* of diamond under compression up to 2 Mbar (Figure S26). As expected from the relationship between the hardness and the bulk modules, these are positively correlated (right). ΔE* of diamond correlates linearly with the bulk modulus (left). Though phenomenological, the observed trend indicates that the hardness of diamond can also be positively correlated with ΔE*.

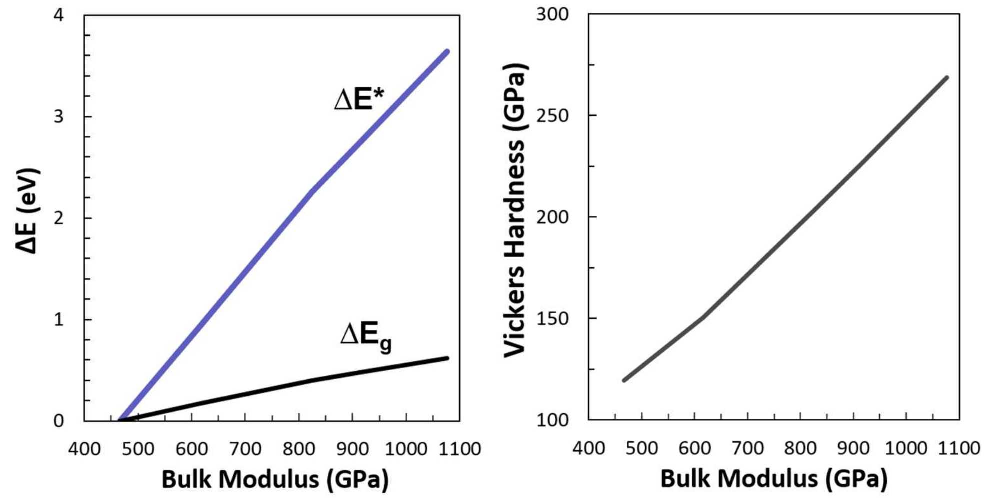

Fig. S26. **Relationship between bulk modulus, changes in E* position, and Vickers hardness of diamond at high pressure up to 2 Mbar. Left.** Relationship between bulk modulus and changes in E* position with respect to that at 1atm (ΔE*). **Right.** Relationship between bulk modulus (*38*) and Vickers hardness of diamond at high pressure up to 2 Mbar. Vickers hardness is estimated from the earlier macroscopic relationship between the properties (*72*).

Fig. S27-left shows the effect of pressure on Mulliken overlap population in diamond with increasing pressure. The overlap population increases *gradually* as pressure increases. Such increase indicates a gradual increase in electronic interaction.

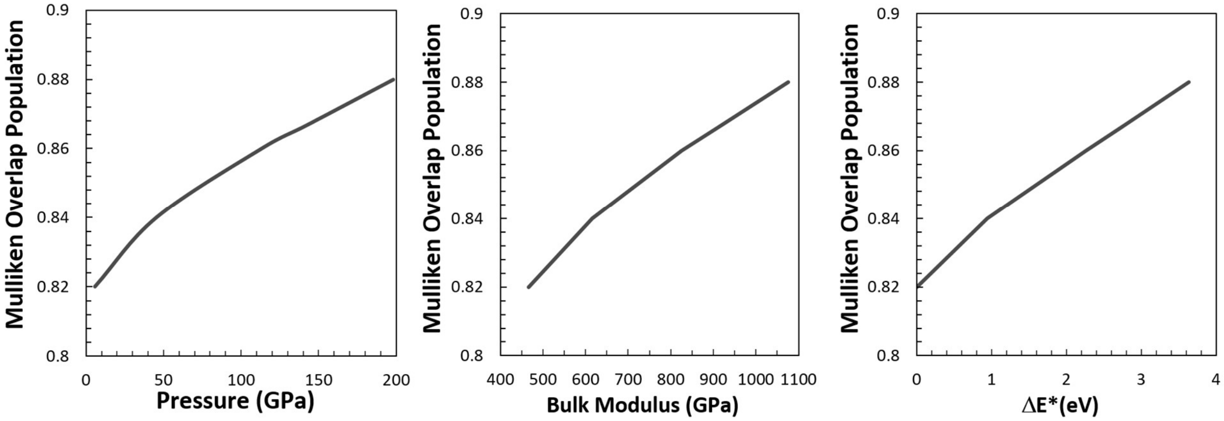

Fig. S27. **Relations among Mulliken overlap population, bulk modulus, and E* position of diamond under compression.** Effect of pressure on Mulliken overlap population in diamond with increasing pressure (left). Relationships between bulk modulus (middle), E* position with respect to that 1 atm (ΔE*) (right).

F. Relationship between diamond-edge Raman peak position and carbon K-edge IXS peak positions of the compressed diamond

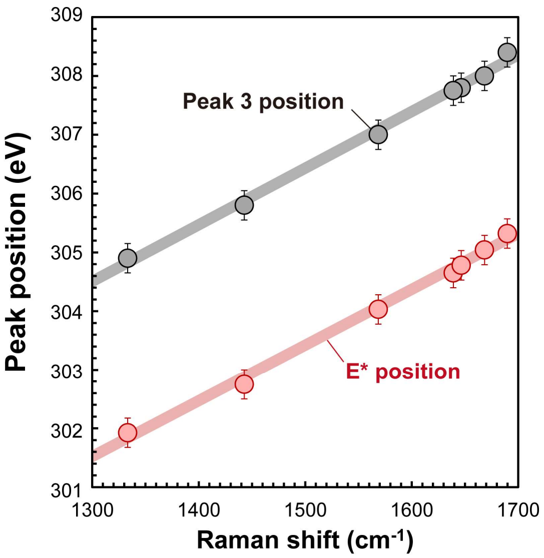

Fig. S28. **Relationship between diamond-edge Raman peak position and pressure-driven peak shifts in the carbon K-edge inelastic x-ray scattering (IXS) spectra for diamond up to 200 GPa.**

Assessment of the practical utility of E* as a pressure indicator. We have shown that position of E* provides a useful pressure indicator at high pressure above megabar. High quality C K-edge measurement around E* for diamond under compression can be performed within ~20 minutes during IXS scans for other edges. While this is certainly long for the pressure estimation, yet is acceptable time scale for IXS measurement. With a further advance in X-ray optics, the collection time will be greatly reduced, increasing its utility as efficient pressure indicator. We also provided detailed simulation results for C K-edge spectrum for diamond with pressure and varying degree of anisotropic compression (see SM-C above), where the E* position does not depend on the nature of anisotropic compression. The uncertainty (mostly depends on the resolution of the C K-edge IXS measurement) is ~5 GPa above megabar pressure conditions. The current IXS-based protocol can be efficient and complimentary pressure gauge for the IXS experiment above multi-megabar pressure conditions. This aspect will be further addressed in our future manuscript.

G. Carbon K-edge IXS spectral image for diamond anvil at 120 GPa

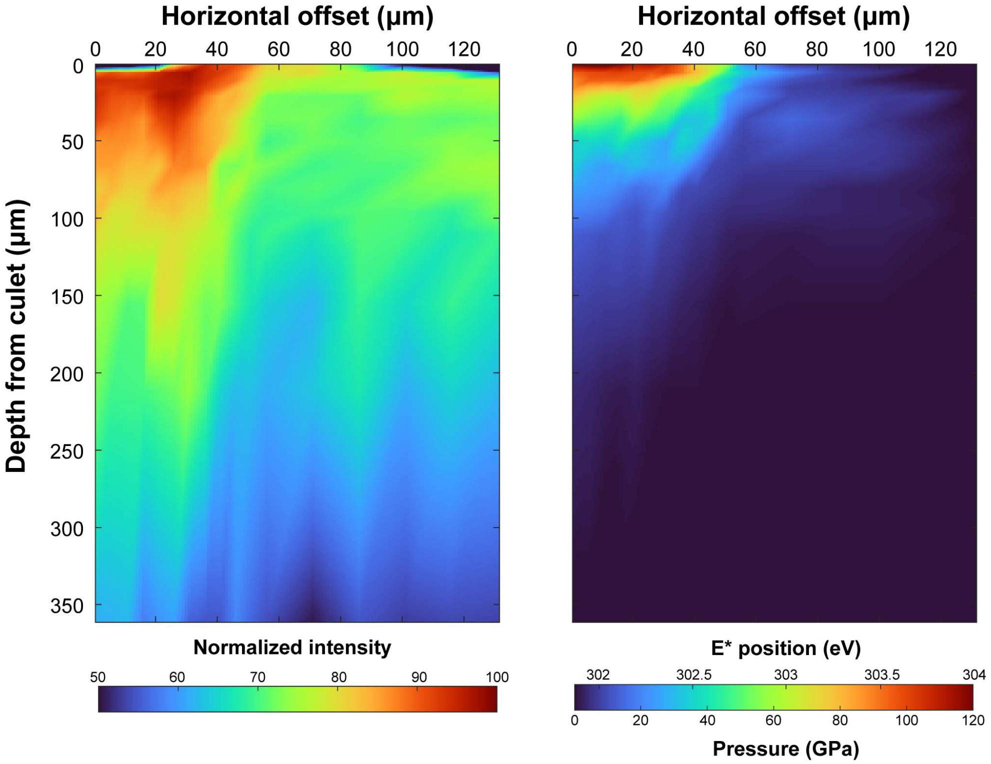

Fig. S29. **Carbon K-edge IXS spectral image for diamond anvil at 120 GPa without rescaling.** **Right.** Two-dimensional image of C K-edge IXS spectral intensity of diamond at 120 GPa. **Left.** The shape of the compressed diamond can be also seen from the IXS intensity map.

REFERENCES

1. A. Lazicki, D. McGonegle, J. R. Rygg, D. G. Braun, D. C. Swift, M. G. Gorman, R. F. Smith, P. G. Heighway, A. Higginbotham, M. J. Suggit, D. E. Fratanduono, F. Coppari, C. E. Wehrenberg, R. G. Kraus, D. Erskine, J. V. Bernier, J. M. McNaney, R. E. Rudd, G. W. Collins, J. H. Eggert, J. S. Wark, Metastability of diamond ramp-compressed to 2 terapascals. *Nature* **589**, 532–535 (2021).

2. Q. Hu, B. Li, X. Gao, Y. Bi, L. Su, H.-K. Mao, Ultrasound elasticity of diamond at gigapascal pressures. *Proc. Natl. Acad. Sci. U.S.A.* **118**, e2118490118 (2021).

3. C. Anzolini, F. Nestola, M. L. Mazzucchelli, M. Alvaro, P. Nimis, A. Gianese, S. Morganti, F. Marone, M. Campione, M. T. Hutchison, J. W. Harris, Depth of diamond formation obtained from single periclase inclusions. *Geology* **47**, 219–222 (2019).

4. R. M. Hazen, R. T. Downs, A. P. Jones, L. Kah, Carbon mineralogy and crystal chemistry, in *Carbon in Earth,* R. M. Hazen, A. P. Jones, J. A. Baross, Eds. (Reviews in Mineralogy and Geochemistry, Mineralogical Society of America, 2013), vol. 75, pp. 7–46.

5. M. J. Walter, S. C. Kohn, D. Araujo, G. P. Bulanova, C. B. Smith, E. Gaillou, J. Wang, A. Steele, S. B. Shirey, Deep mantle cycling of oceanic crust: Evidence from diamonds and their mineral inclusions. *Science* **334**, 54–57 (2011).

6. O. Tschauner, S. Huang, S. Yang, M. Humayun, W. Liu, S. N. G. Corder, H. A. Bechtel, J. Tischler, G. R. Rossman, Discovery of davemaoite, $CaSiO_3$-perovskite, as a mineral from the lower mantle. *Science* **374**, 891–894 (2021).

7. Z. Zeng, J. Wen, H. Lou, X. Zhang, L. Yang, L. Tan, B. Cheng, X. Zuo, W. Yang, W. L. Mao, H.-K. Mao, Q. Zeng, Preservation of high-pressure volatiles in nanostructured diamond capsules. *Nature* **608**, 513–517 (2022).

8. F. Nestola, N. Korolev, M. Kopylova, N. Rotiroti, D. G. Pearson, M. G. Pamato, M. Alvaro, L. Peruzzo, J. J. Gurney, A. E. Moore, J. Davidson, $CaSiO_3$ perovskite in diamond indicates the recycling of oceanic crust into the lower mantle. *Nature* **555**, 237–241 (2018).

9. E. M. Smith, S. B. Shirey, S. H. Richardson, F. Nestola, E. S. Bullock, J. Wang, W. Wang, Blue boron-bearing diamonds from Earth’s lower mantle. *Nature* **560**, 84–87 (2018).

10. O. Tschauner, S. Huang, E. Greenberg, V. B. Prakapenka, C. Ma, G. R. Rossman, A. H. Shen, D. Zhang, M. Newville, A. Lanzirotti, K. Tait, Ice-VII inclusions in diamonds: Evidence for aqueous fluid in Earth's deep mantle. *Science* **359**, 1136–1139 (2018).

11. H. Allen-Sutter, E. Garhart, K. Leinenweber, V. Prakapenka, E. Greenberg, S.-H. Shim, Oxidation of the interiors of carbide exoplanets. *Planet. Sci. J.* **1**, 39 (2020).

12. D. K. Bradley, J. H. Eggert, R. F. Smith, S. T. Prisbrey, D. G. Hicks, D. G. Braun, J. Biener, A. V. Hamza, R. E. Rudd, G. W. Collins, Diamond at 800 GPa. *Phys. Rev. Lett.* **102**, 075503 (2009).

13. K. Katagiri, N. Ozaki, Y. Umeda, T. Irifune, N. Kamimura, K. Miyanishi, T. Sano, T. Sekine, R. Kodama, Shock response of full density nanopolycrystalline diamond. *Phys. Rev. Lett.* **125**, 185701 (2020).

14. J. M. Lang, Y. M. Gupta, Experimental determination of third-order elastic constants of diamond. *Phys. Rev. Lett.* **106**, 125502 (2011).

15. R. F. Smith, J. H. Eggert, R. Jeanloz, T. S. Duffy, D. G. Braun, J. R. Patterson, R. E. Rudd, J. Biener, A. E. Lazicki, A. V. Hamza, J. Wang, T. Braun, L. X. Benedict, P. M. Celliers, G. W. Collins, Ramp compression of diamond to five terapascals. *Nature* **511**, 330–333 (2014).

16. H. Tang, X. H. Yuan, Y. Cheng, H. Z. Fei, F. Y. Liu, T. Liang, Z. D. Zeng, T. Ishii, M. S. Wang, T. Katsura, H. W. Sheng, H. Y. Gou, Synthesis of paracrystalline diamond. *Nature* **599**, 605–610 (2021).

17. H. K. Mao, R. J. Hemley, Optical-transitions in diamond at ultrahigh pressures. *Nature* **351**, 721–724 (1991).

18. R. J. Hemley, H. K. Mao, G. Y. Shen, J. Badro, P. Gillet, M. Hanfland, D. Hausermann, X-ray imaging of stress and strain of diamond, iron, and tungsten at megabar pressures. *Science* **276**, 1242–1245 (1997).

19. S. S. Lobanov, V. B. Prakapenka, C. Prescher, Z. Konôpková, H.-P. Liermann, K. L. Crispin, C. Zhang, A. F. Goncharov, Pressure, stress, and strain distribution in the double-stage diamond anvil cell. *J. Appl. Phys.* **118**, 035905 (2015).

20. A. L. Ruoff, H. Luo, Y. K. Vohra, The closing diamond anvil optical window in multimegabar research. *J. Appl. Phys.* **69**, 6413–6416 (1991).

21. W. L. Mao, H. K. Mao, P. J. Eng, T. P. Trainor, M. Newville, C. C. Kao, D. L. Heinz, J. F. Shu, Y. Meng, R. J. Hemley, Bonding changes in compressed superhard graphite. *Science* **302**, 425–427 (2003).

22. S. K. Lee, P. J. Eng, H. K. Mao, Probing of pressure-induced bonding transitions in crystalline and amorphous Earth materials: Insights from X-ray Raman scattering at high pressure, in *Spectroscopic Methods in Mineralology and Materials Sciences*, G. S. Henderson, D. R. Neuville, R. T. Downs, Eds. (Reviews in Mineralogy and Geochemistry, Mineralogical Society of America, 2014), vol. 78, pp. 139–174.

23. C. Sternemann, M. Wilke, Spectroscopy of low and intermediate *Z* elements at extreme conditions: *In situ* studies of Earth materials at pressure and temperature via X-ray Raman scattering. *High Pressure Res.* **36**, 275–292 (2016).

24. Y. S. Yi, H. Khim, Y. H. Kim, S. K. Lee, Spectral proxies for bonding transitions in SiO_2 and $MgSiO_3$ polymorphs at high pressure up to 270 GPa by O *K*-edge x-ray Raman scattering. *Phys. Rev. B* **103**, 214109 (2021).

25. Y. Q. Cai, H. K. Mao, P. C. Chow, J. S. Tse, Y. Ma, S. Patchkovskii, J. F. Shu, V. Struzhkin, R. J. Hemley, H. Ishii, C. C. Chen, I. Jarrige, C. T. Chen, S. R. Shieh, E. P. Huang, C. C. Kao, Ordering of hydrogen bonds in high-pressure Low-Temperature H2O. *Phys. Rev. Lett.* **94**, 025502 (2005).

26. W. Schülke, *Electron Dynamics by Inelastic X-ray Scattering* (OUP Oxford, 2007), vol. 7.

27. Y. Lin, L. Zhang, H. K. Mao, P. Chow, Y. M. Xiao, M. Baldini, J. F. Shu, W. L. Mao, Amorphous diamond: A high-pressure superhard carbon allotrope. *Phys. Rev. Lett.* **107**, 175504 (2011).

28. S. K. Lee, Y. H. Kim, Y. S. Yi, P. Chow, Y. M. Xiao, C. Ji, G. Y. Shen, Oxygen quadclusters in SiO_2 glass above megabar pressures up to 160 GPa revealed by x-ray Raman scattering. *Phys. Rev. Lett.* **123**, 235701 (2019).

29. S. K. Lee, Y.-H. Kim, P. Chow, Y. Xiao, C. Ji, G. Shen, Amorphous boron oxide at megabar pressures via inelastic X-ray scattering. *Proc. Natl. Acad. Sci. U.S.A.* **115**, 5855–5860 (2018).

30. Y. H. Kim, Y. S. Yi, H.-I. Kim, P. Chow, Y. Xiao, G. Shen, S. K. Lee, Structural transitions in $MgSiO_3$ glasses and melts at the core-mantle boundary observed *via* inelastic x-ray scattering. *Geophys. Res. Lett.* **46**, 13756–13764 (2019).

31. G. Y. Shen, Y. B. Wang, A. Dewaele, C. Wu, D. E. Fratanduono, J. Eggert, S. Klotz, K. F. Dziubek, P. Loubeyre, O. V. Fat'yanov, P. D. Asimow, T. Mashimo, R. M. M. Wentzcovitch, J. Bass, Y. Bi, D. W. He, K. V. Khishchenko, K. Leinenweber, B. S. Li, T. Sakai, T. Tsuchiya, K. Shimizu, D. Yamazaki, M. Mezouar; other members of the IPPS task group, Toward an international practical pressure scale: A proposal for an IPPS ruby gauge (IPPS-Ruby2020). *High Pressure Res.* **40**, 299–314 (2020).

32. J. F. Morar, F. J. Himpsel, G. Hollinger, G. Hughes, J. L. Jordan, Observation of a C-1s Core exciton in diamond. *Phys. Rev. Lett.* **54**, 1960–1963 (1985).

33. J. Nithianandam, Synchrotron x-ray photoemission and reflectance study of the dipole forbidden diamond core exciton. *Phys. Rev. Lett.* **69**, 3108–3111 (1992).

34. S. P. Gao, C. J. Pickard, M. C. Payne, J. Zhu, J. Yuan, Theory of core-hole effects in 1s core-level spectroscopy of the first-row elements. *Phys. Rev. B* **77**, 115122 (2008).

35. S. Huotari, T. Pylkkanen, J. A. Soininen, J. J. Kas, K. Hamalainen, G. Monaco, X-ray-Raman-scattering-based EXAFS beyond the dipole limit. *J. Synchrot. Radiat.* **19**, 106–113 (2012).

36. F. J. Himpsel, J. F. Vanderveen, D. E. Eastman, Experimental bulk energy bands for diamond using *hv*-dependent photoemission. *Phys. Rev. B* **22**, 1967–1971 (1980).

37. F. Occelli, P. Loubeyre, R. LeToullec, Properties of diamond under hydrostatic pressures up to 140 GPa. *Nat. Mater.* **2**, 151–154 (2003).

38. F. Zhi-Jian, J. Guang-Fu, C. Xiang-Rong, G. Qing-Quan, First-principle calculations for elastic and thermodynamic properties of diamond. *Commun. Theor. Phys.* **51**, 1129–1134 (2009).

39. F. Gao, J. He, E. Wu, S. Liu, D. Yu, D. Li, S. Zhang, Y. Tian, Hardness of covalent crystals. *Phys. Rev. Lett.* **91**, 015502 (2003).

40. F. M. Gao, L. H. Gao, Microscopic models of hardness. *J. Superhard Mater.* **32**, 148–166 (2010).

41. A. Mansouri Tehrani, J. Brgoch, Hard and superhard materials: A computational perspective. *J. Solid State Chem.* **271**, 47–58 (2019).

42. V. A. Mukhanov, O. O. Kurakevych, V. L. Solozhenko, Thermodynamic model of hardness: Particular case of boron-rich solids. *J. Superhard Mater.* **32**, 167–176 (2010).

43. V. L. Solozhenko, E. Gregoryanz, Synthesis of superhard materials. *Mater. Today* **8**, 44–51 (2005).

44. J. S. Tse, Intrinsic hardness of crystalline solids. *J. Superhard Mater.* **32**, 177–191 (2010).

45. M. D. Segall, R. Shah, C. J. Pickard, M. C. Payne, Population analysis of plane-wave electronic structure calculations of bulk materials. *Phys. Rev. B Condens. Matter.* **54**, 16317–16320 (1996).

46. Y. Akahama, H. Kawamura, Diamond anvil Raman gauge in multimegabar pressure range. *High Pressure Res.* **27**, 473–482 (2007).

47. R. Vogelgesang, A. K. Ramdas, S. Rodriguez, M. Grimsditch, T. R. Anthony, Brillouin and Raman scattering in natural and isotopically controlled diamond. *Phys. Rev. B Condens. Matter.* **54**, 3989–3999 (1996).

48. R. Maezono, A. Ma, M. D. Towler, R. J. Needs, Equation of state and raman frequency of diamond from quantum Monte Carlo simulations. *Phys. Rev. Lett.* **98**, 025701 (2007).

49. J. S. Tse, W. B. Holzapfel, Equation of state for diamond in wide ranges of pressure and temperature. *J. Appl. Phys.* **104**, 043525 (2008).

50. P. Chow, Y. M. Xiao, E. Rod, L. G. Bai, G. Y. Shen, S. Sinogeikin, N. Gao, Y. Ding, H.-K. Mao, Focusing polycapillary to reduce parasitic scattering for inelastic x-ray measurements at high pressure. *Rev. Sci. Instrum.* **86**, 072203 (2015).

51. Y. H. Kim, Y. S. Yi, H.-I. Kim, P. Chow, Y. Xiao, G. Shen, S. K. Lee, Pressure-driven changes in the electronic bonding environment of GeO_2 glass above megabar pressures. *J. Am. Chem. Soc.* **144**, 10025–10033 (2022).

52. S. J. Clark, M. D. Segall, C. J. Pickard, P. J. Hasnip, M. I. J. Probert, K. Refson, M. C. Payne, First principles methods using CASTEP. *Z. Kristallogr. Cryst. Mater.* **220**, 567–570 (2005).

53. J. P. Perdew, K. Burke, M. Ernzerhof, Generalized gradient approximation made simple. *Phys. Rev. Lett.* **77**, 3865–3868 (1996).

54. Y. S. Yi, S. K. Lee, Atomistic origins of pressure-induced changes in the O *K*-edge x-ray Raman scattering features of Si O_2 and MgSi O_3 polymorphs: Insights from *ab initio* calculations. *Phys. Rev. B* **94**, 094110 (2016).

55. I. Mosyagin, D. Gambino, D. G. Sangiovanni, I. A. Abrikosov, N. M. Caffrey, Effect of dispersion corrections on *ab initio* predictions of graphite and diamond properties under pressure. *Phys. Rev. B* **98**, 174103 (2018).

56. J.-P. Rueff, A. Shukla, Inelastic x-ray scattering by electronic excitations under high pressure. *Rev. Mod. Phys.* **82**, 847 (2010).

57. P. Blaha, K. Schwarz, F. Tran, R. Laskowski, G. K. H. Madsen, L. D. Marks, WIEN2k: An APW+lo program for calculating the properties of solids. *J. Chem. Phys.* **152**, 074101 (2020).

58. T. Mizoguchi, I. Tanaka, S.-P. Gao, C. J. Pickard, First-principles calculation of spectral features, chemical shift and absolute threshold of ELNES and XANES using a plane wave pseudopotential method. *J. Phys. Condens. Matter* **21**, 104204 (2009).

59. J. Zemann, *Crystal Structures, 2nd edition, Vol. 1 by R. W. G. Wyckoff* (Acta Crystallographica, 1965), vol. 18, pp. 139.

60. M. P. Surh, S. G. Louie, M. L. Cohen, Band gaps of diamond under anisotropic stress. *Phys. Rev. B Condens Matter.* **45**, 8239–8247 (1992).

61. A. L. Ruoff, H. Luo, Pressure strengthening: A possible route to obtaining 9 Mbar and metallic diamonds. *J. Appl. Phys.* **70**, 2066–2070 (1991).

62. G. Bertoni, L. Calmels, A. Altibelli, V. Serin, First-principles calculation of the electronic structure and EELS spectra at the graphene/Ni(111) interface. *Phys. Rev. B* **71**, 075402 (2005).

63. Y. Meng, H.-k. Mao, P. J. Eng, T. P. Trainor, M. Newville, M. Y. Hu, C. Kao, J. Shu, D. Hausermann, R. J. Hemley, The formation of sp^3 bonding in compressed BN. *Nat. Mater.* **3**, 111–114 (2004).

64. W. Pabst, E. Gregorova, Elastic properties of silica polymorphs—A review. *Ceramics - Silikaty* **57**, 167–184 (2013).

65. D. Andrault, G. Fiquet, F. Guyot, M. Hanfland, Pressure-induced Landau-type transition in stishovite. *Science* **282**, 720–724 (1998).

66. L.-G. Liu, Bulk moduli of SiO_2 polymorphs: Quartz, coesite and stishovite. *Mech. Mater.* **14**, 283–290 (1993).

67. A. R. Oganov, M. J. Gillan, G. D. Price, Structural stability of silica at high pressures and temperatures. *Phys. Rev. B* **71**, 064104 (2005).

68. Z. Zhang, L. Stixrude, J. Brodholt, Elastic properties of $MgSiO_3$-perovskite under lower mantle conditions and the composition of the deep Earth. *Earth Planet. Sci. Lett.* **379**, 1–12 (2013).

69. X. Jiang, J. Zhao, X. Jiang, Correlation between hardness and elastic moduli of the covalent crystals. *Comput. Mate. Sci.* **50**, 2287–2290 (2011).

70. F. Gao, Theoretical model of intrinsic hardness. *Phys. Rev. B* **73**, 132104 (2006).

71. K. Li, X. Wang, F. Zhang, D. Xue, Electronegativity identification of novel superhard materials. *Phys. Rev. Lett.* **100**, 235504 (2008).

72. V. A. Mukhanov, O. O. Kurakevych, V. L. Solozhenko, Hardness of materials at high temperature and high pressure. *Philos. Mag.* **89**, 2117–2127 (2009).

73. Q. Zhu, A. R. Oganov, M. A. Salvadó, P. Pertierra, A. O. Lyakhov, Denser than diamond: *Ab initio* search for superdense carbon allotropes. *Phys. Rev. B* **83**, 193410 (2011).

74. T. Mizoguchi, Overlap population diagram for ELNES and XANES: Peak assignment and interpretation. *J. Phys. Condens. Matter* **21**, 104215 (2009).

75. A. Šimůnek, J. Vackář, Hardness of covalent and ionic crystals: First-principle calculations. *Phys. Rev. Lett.* **96**, 085501 (2006).

76. S.-Q. Feng, Y. Yang, J.-Y. Li, X.-X. Jiang, H.-N. Li, X.-L. Cheng, Pressure effect on the hardness of diamond and W_2B_5: First-principle calculations. *Mod. Phys. Lett. B* **31**, 1750137 (2017).